Emergent structure and dynamics of tropical forest-grassland landscapes

Bert Wuyts and Jan Sieber
College of Engineering, Mathematics and Physical Sciences, University of Exeter, EX4 4QF, UK

arXiv:2207.14118v2 [q-bio.PE] 1 Mar 2023

It is thought that tropical forests can exist as an alternative stable state to savanna [1, 2]. Therefore, perturbation by climate change or human impact may lead to crossing of a tipping point beyond which there is rapid large-scale forest dieback that is not easily reversed [3–5]. Empirical evidence for bistability due to fire-vegetation feedbacks relies on tree cover bimodality in satellite-observed data [1, 2], but this may also be explained by spatial heterogeneity [6], or by biases in the data [7, 8]. Theoretical evidence for bistability [9–11] does not consider the interaction of fire with the vegetation landscape. Focusing on landscapes consisting of tropical forest and grassland, we show that the microscopic rules of fire and vegetation spread [as proposed by 12] lead to an emergent relation between macroscopic forest structure and dynamics. This relation defines a landscape-scale balance equation of forest area change in which the forest perimeter determines the nonlinearity in forest growth while the forest perimeter weighted by adjacent grassland area determines the nonlinearity in forest loss. We demonstrate that our equation enables analysis of resilience or abrupt shifts for a given landscape, using only the landscape state at a single point in time and measurable parameters of the underlying microscopic spatial processes, thereby avoiding the problems associated with reliance on bimodality.

INTRODUCTION

Satellite observations of tropical tree cover show that in a wide range of mean annual rainfall [1, 2], both savanna (low tree cover) and forest (high tree cover) are possible, making the distribution of tree cover *bimodal*. On the one hand, fire exclusion experiments show that fire can maintain low tree cover [13]. On the other hand, fire occurs almost exclusively below a tree cover threshold of about 40% [1, 6, 14–16], which is consistent with fire being a *percolation* process [17, 18] on grass patches [10, 19]. Such a highly nonlinear response of fire to grass together with an empirically consistent response of vegetation to fire was shown to be sufficient for inducing *bistability* in simple models [9]. Taken together, the bimodality, the mutual interaction between fire and vegetation, and the availability of a plausible underlying mechanism provide compelling evidence that forest and savanna are *alternative stable states*, maintained by a feedback between vegetation and fire [1], and between which transitions would neither be gradual nor easily reversed [3, 5]. Exploiting the link between the probability distribution and stability, one has thus been able to quantify forest resilience at given environmental conditions [2]. However, subsequent work called into question the reliance on bimodality of spatial data to study bistability and resilience of tropical forests, showing that at least part of the bimodality can be explained by independent spatial heterogeneity of variables other than mean annual rainfall [6], or by data artefacts [7, 8]. Therefore, further empirical work on bistability and resilience of tropical forests should ideally concentrate on processes or quantities that are closely linked to the assumed underlying processes leading to bistability.

Even though fire percolation on flammable vegetation patches is assumed to underlie bistability, models proposed as theoretical evidence for this mechanism have not modelled fire explicitly, neither in mean-field models [9, 16, 20–22], nor in microscopic simulation models [10, 11]. Their approach relies on two key assumptions: (i) fire acts on a *much faster timescale* than vegetation, (ii) fire-blocking tree patches are spatially *well mixed* with flammable patches. If one assumes point (i), the effects of fire are determined by the vegetation landscape. If one also assumes point (ii), the spatial arrangement of patches becomes irrelevant, such that the effect of fire on a given tree species scales with the product of the expected fire size and the cover fraction of the considered species. Assumption (ii) further makes the expected fire size depend only on total flammable species cover, with the dependence inferable from percolation theory. In *mean-field models* [9, 16, 20], patches of all considered vegetation species are assumed to be well mixed in a large homogeneous landscape ($N\to\infty$), such that the dynamics depend deterministically on the landscape fraction covered by each species, with the interaction between any two species written as the product of their cover fractions. In this manner, mean-field models only require as many equations as there are species and are thus easy to analyse. Spatial mean-field models [11, 21, 22] permit spatial variation on the mesoscopic scale but still rely on a well-mixedness assumption between the mesoscopic and macroscopic scales. While mean-field models are usually qualitatively correct, it is well known that assuming well-mixedness results in neglect of spatial structure, leading to biases in regimes where structure is important [e.g. 23, 24]. The importance of spatial structure (and hence the bias of mean-field models) can be examined via *microscopic simulation models*, such as cellular automata or interacting particle systems. These consider the detailed spatiotemporal dynamics by applying microscopic interaction rules to cells or individuals of one or more species in a spatial domain. Although microscopic models have been in use for simulation of fire spread for some time [25], and some have investigated the interplay between fire and vegetation dynamics in the tropics [e.g.

12, 26–28], most microscopic models focusing on tropical tree cover bistability do not model fire explicitly, implementing only the microscopic rules of vegetation spread (10, 11; excepting 12). Instead, they captured the effects of fire similarly as in mean-field models, relying on an assumption of well-mixedness on the macroscopic [10] or mesoscopic [11] scale. Therefore, they only show the spatial structure associated with vegetation dynamics, and not that related to fire. Of the few exceptions that model fire explicitly as a percolation process [12, 29], only the model by Hébert-Dufresne *et al.* [12] is fully microscopic, while that by Staal *et al.* [29] uses a spatial mean-field model for the vegetation component. Besides bistability, Hébert-Dufresne *et al.* found an equilibrium perimeter-area power-law relation of isolated forest patches consistent with data from protected Brazilian savannas. Yet, they analysed landscape-scale dynamics based on the mean-field approximation of their microscopic model, i.e. disregarding spatial structure. Altogether, it is thus still poorly understood how the interplay of fire and spatial vegetation structure in the tropics affects landscape dynamics, and how it modifies or contributes to alternative stable tree cover states.

In this work, we use the microscopic model of tropical forest and fire proposed by Hébert-Dufresne et al. [12] to examine the importance of spatial structure that emerges from the interplay of fire and vegetation dynamics, including its consequences for resilience and bistability. We observe in simulations that forest gain due to nearby dispersal and forest loss due to fire occur at the forest perimeter instead of in a well-mixed fashion. This leads us to a macroscopic balance equation of forest area change (Eq. 9) which takes into account the effect of dispersal and fire on the forest perimeter, while still assuming timescale separation between fire and forest dynamics. Our balance equation permits us to assess forest resilience only from the landscape state at a single point in time and the parameters of the microscopic processes (Table M1). We verify the assumptions of timescale separation and well-mixedness ((*i*) and (*ii*) above) in detail in the Supplementary Information, and find that the former is plausible for realistically sized systems while the latter is strongly violated, particularly near the tipping threshold. Hence, this renders mean-field models incapable of predicting events such as forest dieback. However, as (for our parameter choices) the alternative stable states lie in the well-mixed regime, mean-field models still permit explicit expressions for their dependence on parameters and for the minimum fire ignition rate for onset of bistability.

RESULTS

The FGBA probabilistic cellular automaton

The FGBA probabilistic cellular automaton (adapted from [12] – see Fig. 1 and Methods) models the stochastic dynamics of tropical vegetation and fire on a square lattice and in continuous time. The key empirical facts of tropical forest and fire dynamics captured by the FGBA automaton are: (*i*) fires only naturally ignite in grasslands but they can spread into forest, (*ii*) fires spread faster in grassland than in forest, such that forests suppress fires, albeit imperfectly, (*iii*) forest dynamics occurs on a *strongly separated timescale* from fire spread and grass regrowth.

This results in the following reaction rules in the cellular automaton. At any time, each lattice cell can be in one of four states: F – forest, G – grass, B – burning, A – ash. Conversions between these states can occur spontaneously or due to spread to neighbouring cells (Fig. 1a and Table M1). The spontaneous conversions are: forest recruitment on grass or ash cells due to long-distance seed dispersal or from a homogeneous seed bank (G $\to$ F or A $\to$ F at rate β), forest mortality (F $\to$ G at rate γ), fire ignition on grass cells (G $\to$ B at rate ϕ), and grass regrowth on ash cells (A $\to$ G at rate λ). The conversions due to spread to neighbours are: forest recruitment due to short-distance seed dispersal on grass or ash cells (GF $\to$ FF, AF $\to$ FF at rate α), fire spread on grass (GB $\to$ BB at rate ρ_{g}) or on tree cells (FB $\to$ BB at rate ρ_{f}). Chosen parameters are in the ranges empirically justified by [12] for a square domain of 100x100 cells, with cell size Δx=Δy=30m. The timescale separation between fire and forest dynamics implies that the rates satisfy $\rho_{\mathrm{g}}, \rho_{\mathrm{f}}, \mu, \lambda \gg \alpha, \beta, \gamma$. In particular, we choose

$$\rho_{\mathrm{g}}, \mu \sim 10^6 > \rho_{\mathrm{f}} \sim 10^5 \gg 1\mathrm{y}^{-1}, \tag{1}$$

$$\alpha, \beta, \gamma \sim 10^{[-4,-2]} \ll \lambda \sim 1\mathrm{y}^{-1}. \tag{2}$$

So, fire spreading and extinction ρ_{g}, ρ_{f}, μ occur on the scale of hours, while grass regrows on ash over months (λ) and forest spread, growth and mortality α, β, γ occurs over decades. We take fire ignition rate $\phi \sim 1/N$ such that fires spontaneously occur about once per year in the modelled area. Figure 1b–d shows a typical time profile for fractions of cells in each state. The initial state is all grass and the ignition rate ϕ is low, such that a nearly closed canopy state is the only steady state (reached after 300 years, Fig. 1h). Brief events of rapidly spreading fire counteract a gradual spread of forest. Timescale separation of forest dynamics (Fig. 1b), grass regrowth (Fig. 1c), and fire spread (Fig. 1d) shows clearly.

Figure 2a shows a bifurcation diagram of steady state forest area in the FGBA cellular automaton, denoted by [F] (see Eq. M1), versus fire ignition rate ϕ. Unstable steady states (saddles) were obtained by applying feedback control to the simulations (see Methods). *Bistability* occurs above a critical ignition rate ϕ, with as alternative stable states grassland ([F]$\approx$0) and forest ([F]$\approx$0.83). Simulations initiated at the saddle will tip up or down depending on initial stochasticity (Fig. 2b). Near the lower end of the bistability range, the saddle solution is fairly homogeneous, but for higher ϕ values, a single hole of grass in forest arises (insets in Fig. 2a).

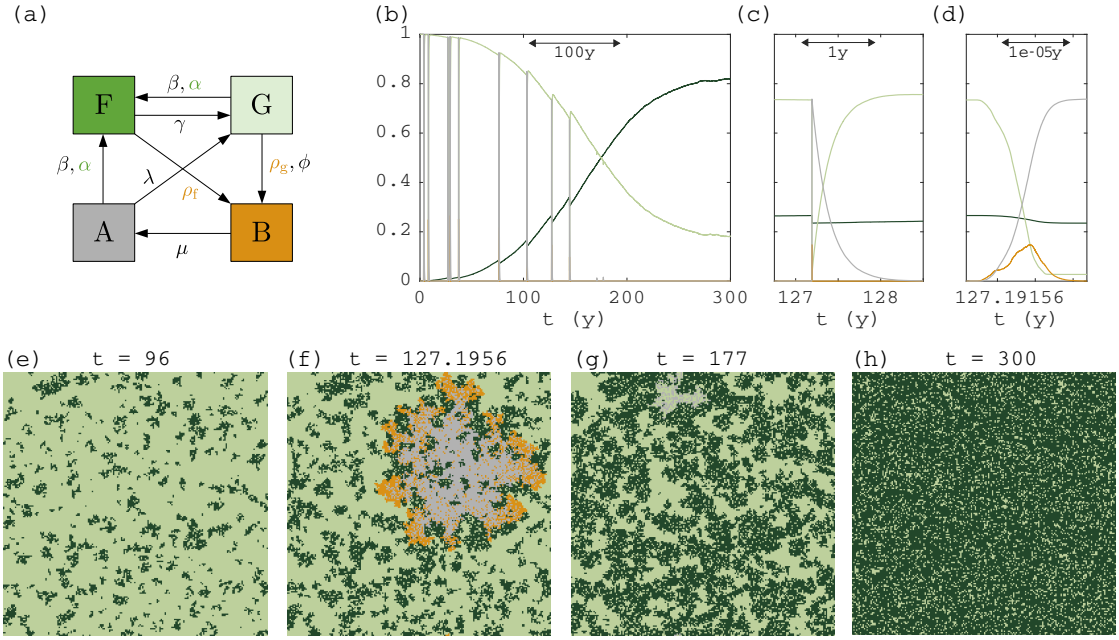

FIG. 1. The FGBA stochastic cellular automaton: (a) state transition diagram (coloured rates: spread to neighbouring cell, black rates: spontaneous conversion within cell), (b) example time series of a simulation starting at zero tree cover, (c,d) 10x and 10^7x zoom of (b), (e-h) snapshots of a simulation at indicated times for low fire ignition rate (ϕN=0.075). The fire in (f) spreads throughout grassland in the whole domain whereas that in (g) went extinct locally because forest splits grassland in clusters (notice the area of ash near the top). Remaining parameters are shown in Table M1. Domain size: 200x200 cells.

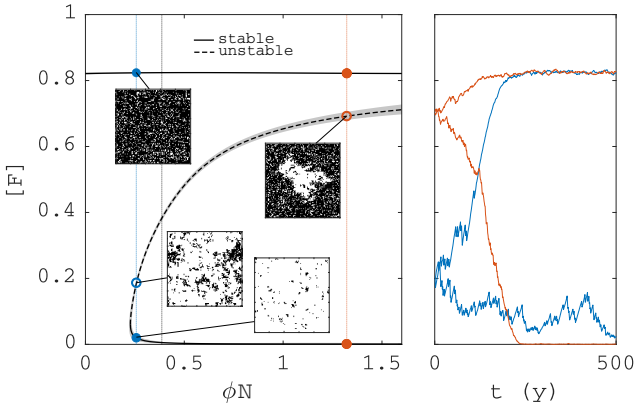

FIG. 2. Steady states and bistability of forest area in the FGBA cellular automaton. (a) Bifurcation diagram of forest area fraction [F] versus fire ignition rate ϕ (shade: two-standard deviation confidence interval of the mean). (b) Simulations initiated at two different points on the saddle (ϕN=0.257 and ϕN=1.32). Remaining parameters are shown in Table M1. Domain size: 100x100 cells.

Fast and slow subprocesses

The timescale separation (Eqs. 1 and 2) permits treatment of the joint vegetation and fire dynamics as a fast-slow system. Fire spread occurs on the fast timescale, where the vegetation landscape is treated as constant. Forest dynamics occurs on the slow timescale, where the effects of fire are a steady state function of the vegetation landscape.

Fast process: fires spreading in a given landscape On the timescale of a single fire event, forest dynamics are negligible ($\alpha, \beta, \gamma \ll 1/\text{day}$) such that we can consider the total landscape of forest patches as fixed. For each ignition event, this results in the following dynamics. A fire ignites on a grass cell, then spreads across its grassland cluster at a rate ρ_g per BG pair, after which it reaches the interface with adjacent forest, where it starts intruding the forest at a rate ρ_f per BF pair. At any time, a burning cell can stop burning spontaneously, converting to ash at a rate μ. The probabilities of fire spreading into a neighbouring grass or forest cell before the originating cell stops burning are given by

$$p_\text{g} := \frac{\rho_\text{g}}{\rho_\text{g} + \mu} = 0.9, \qquad p_\text{f} := \frac{\rho_\text{f}}{\rho_\text{f} + \mu} = 0.1, \tag{3}$$

where we have shown the chosen values in our simulations [adopted from 12]. Since regrowth of grass and ignition of new fires occur at a much slower rate than fire spread ($\phi N \lesssim \lambda \ll \rho_\text{f}, \mu, \rho_\text{g}$) and our domain is relatively small (see Section S2B), we observe repeated fire spreading events well separated in time (Fig. 1b), each ending with spontaneous extinction.

When a fire in grassland cluster with index j reaches its interface with adjacent forest, the resulting forest loss due to this single fire event can be approximated as (see Methods):

$$\Delta^\text{loss}_{\text{F},j} := p_\text{f}[\text{FG}]_j, \tag{4}$$

where $[\mathrm{FG}]_j$ counts the number of forest cells adjacent to grassland cluster j (with both sides of the equation optionally normalised by N). This approximation relies on the assumptions that the fire reaches the whole interface with forest (i.e. $p_\mathrm{g} \to 1$) and only once per fire (i.e. $\rho_\mathrm{g} \gg \lambda \gg \phi N$), and that p_f is small.

Slow processes: forest demography and fire damage Forest demography and loss due to repeated fires occur on the slow timescale. Writing the number of forest-grass neighbour pairs as [FG] (divided by N, equivalently the total perimeter of forest or grass patches, see Eq. M1), the dynamics for tree recruitment and mortality result in an expected rate of change for [F]:

$$\Delta_\mathrm{F}^\mathrm{gain} := \beta[\mathrm{G}] - \gamma[\mathrm{F}] + \alpha[\mathrm{FG}]. \tag{5}$$

In Eq. 5, the rates of change are $\beta[\mathrm{G}]$ for spontaneous forest growth on grass, $\gamma[\mathrm{F}]$ for spontaneous forest mortality, and $\alpha[\mathrm{FG}]$ for spread of forest into grass at its perimeter.

The rate of forest erosion at its perimeter due to fire damage over many fire events is the weighted sum over all grass clusters j=1, ..., n_c, i.e.

$$\Delta_\mathrm{F}^\mathrm{loss} := \sum_{j=1}^{n_\mathrm{c}} \phi N [\mathrm{G}]_j \Delta_{\mathrm{F},j}^\mathrm{loss} = \phi N p_\mathrm{f} \sum_{j=1}^{n_\mathrm{c}} [\mathrm{G}]_j [\mathrm{FG}]_j, \tag{6}$$

where $[\mathrm{G}]_j$ is the fraction of G cells in grass cluster j (so, $[\mathrm{G}]=\sum_{j=1}^{n_\mathrm{c}} [\mathrm{G}]_j$), $\phi N[\mathrm{G}]_j$ is the rate at which fires spontaneously ignite in grass cluster j (ϕ is the rate per cell and $N[\mathrm{G}]_j$ is the area of the cluster), and $\Delta_{\mathrm{F},j}^\mathrm{loss}=p_\mathrm{f}[\mathrm{FG}]_j$ is the conversion of forest to ash caused by each fire event (see Eq. 4) (note also that $[\mathrm{FG}]=\sum_{j=1}^{n_\mathrm{c}} [\mathrm{FG}]_j$). By defining the *grassland-weighted forest perimeter* as

$$\langle[\mathrm{FG}]\rangle_\mathrm{cg} := \sum_{j}^{n_\mathrm{c}} \frac{[\mathrm{G}]_j}{[\mathrm{G}]} [\mathrm{FG}]_j, \tag{7}$$

the expression for forest loss becomes

$$\Delta_\mathrm{F}^\mathrm{loss} = \phi\, p_\mathrm{f}\, N[\mathrm{G}]\langle[\mathrm{FG}]\rangle_\mathrm{cg}. \tag{8}$$

The grassland-weighted forest perimeter $\langle[\mathrm{FG}]\rangle_\mathrm{cg}$ is the average perimeter of forest clusters weighted by the relative size of their adjacent grass cluster.

Emergent slow dynamics

We now form the balance between the slow processes discussed above, assuming fire converts trees immediately to grass (i.e. $\lambda \gg \phi N$). The resulting expected rate of forest area change during a short time interval is

$$\begin{aligned} \langle\frac{\mathrm{d}[\mathrm{F}]}{\mathrm{d}t}\rangle &= \Delta_\mathrm{F}^\mathrm{gain} - \Delta_\mathrm{F}^\mathrm{loss}, \\ \frac{\mathrm{d}[\mathrm{F}]}{\mathrm{d}t} &= \beta[\mathrm{G}] - \gamma[\mathrm{F}] + \alpha[\mathrm{FG}] - \phi p_\mathrm{f} N[\mathrm{G}]\langle[\mathrm{FG}]\rangle_\mathrm{cg}, \end{aligned} \tag{9}$$

where we used Eqs. 5 and 8, and assumed on the left-hand side that N is sufficiently large, such that, via the law of large numbers, $\langle \mathrm{d}[\mathrm{F}]/\mathrm{d}t\rangle \approx \mathrm{d}[\mathrm{F}]/\mathrm{d}t$. Equation 9 can be understood intuitively as forest and grass competing for space within clusters (spontaneous terms) and at their interface (interaction terms). A larger interface [FG] leads simultaneously to faster forest spread (proportional to its perimeter [FG]), and to increased exposure to fires (proportional to its grassland-weighted perimeter $\langle[\mathrm{FG}]\rangle_\mathrm{cg}$). Fires are most damaging to forest when [G] forms a single cluster, i.e. $\langle[\mathrm{FG}]\rangle_\mathrm{cg}$=[FG], such that each fire reaches the whole interface. Conversely, when forest patches break [G] into several clusters $\langle[\mathrm{FG}]\rangle_\mathrm{cg}$ is smaller than [FG], such that several ignitions are required to have the same effect, slowing forest erosion down. Additionally, the total amount of grass $N[\mathrm{G}]$ determines the number of ignitions and hence the rate at which grass spreads into forest. The parameters determine the relative weight of each of the discussed effects.

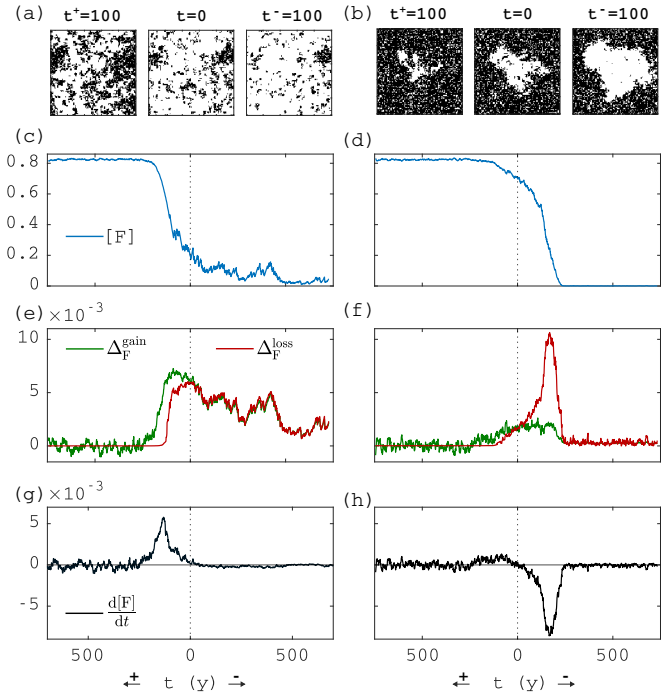

FIG. 3. Rate of change according to Eq. 9. (a,b) Spatial snapshots at indicated times, (c,d) time series of [F], (e,f) time series of $\Delta_\mathrm{F}^\mathrm{gain}$, $\Delta_\mathrm{F}^\mathrm{loss}$, (g,h) time series of the right-hand side of Eq. 9 (gain minus loss). At t=0, the simulation is started on the saddle (on the left, [F](0) $\approx$ 0.2 and on the right, [F](0) $\approx$ 0.7, see blue and red circles in Fig. 2). Towards the left (along t^+), a simulation that tips up and towards the right (along t^-) a simulation that tips down is shown. Parameters are shown in Table M1. Columns correspond to leftmost and rightmost vertical dashed lines in Fig. 2 (ϕN=0.257 and ϕN=1.32). Domain size: 100x100 cells.

Figure 3 shows example simulations along trajectories starting from the saddle equilibria of Fig. 2, showing forest area [F] in space and time (a–d), the gain/loss terms $\Delta_\mathrm{F}^\mathrm{gain}$ and $\Delta_\mathrm{F}^\mathrm{loss}$ defined in Eqs. 5 and 8 (e–f), and the right-hand side of Eq. 9 (gain minus loss, g–h). The left

column of Fig. 3 shows simulations for low fire ignition rate ϕ and low [F](0), and the right column for high ϕ and high [F](0). Each column shows two realisations, both starting from the same saddle steady state. One realisation evolves toward high forest cover, shown on axis t^+ (increasing to the left from t=0), the other realisation evolves toward low forest cover, shown on axis t^- (increasing to the right from t=0). In the stable steady states, gain (green) and loss (red) terms vary around the same mean. On the saddle (at t=0), gain and loss functions cross, indicating that the steady states and changes are accurately captured by Eq. 9. The largest changes in forest cover [F] occur when there are large changes in forest loss due to fire. The snapshots in Fig. 3a,b show that the high-cover state changes as an expanding/contracting hole in the forest, whereas the low-cover state is more homogeneous.

Emergent nonlinear relations

Equation 9 explains how the rate of change of [F] depends on the perimeter quantities [FG] and $\langle[\mathrm{FG}]\rangle_{\mathrm{cg}}$. Figure 4a–c shows a scatterplot of [FG](t) and $\langle[\mathrm{FG}]\rangle_{\mathrm{cg}}(t)$ versus [F](t) for three different values of ϕ, and for an ensemble of simulations starting from the saddle in Fig. 2a, with each point being a value observed at a discrete observation time. Remarkably, we observe that [FG] and $\langle[\mathrm{FG}]\rangle_{\mathrm{cg}}$ lie on a narrow band around some steady state functions $[\mathrm{FG}]^*$ and $\langle[\mathrm{FG}]\rangle^*_{\mathrm{cg}}$ of [F] (and ϕ), which implies that [FG], $\langle[\mathrm{FG}]\rangle_{\mathrm{cg}}$ are changing on a much faster timescale, making them slaved to [F]. Figure 4d–f shows the terms on the right-hand side of Eq. 9 depending on [F], splitting between gain and loss terms $\Delta_{\mathrm{F}}^{\mathrm{gain}}, \Delta_{\mathrm{F}}^{\mathrm{loss}}$, as defined in Eqs. 5 and 8. Steady states occur when gain equals loss ($\Delta_{\mathrm{F}}^{\mathrm{gain}}$=$\Delta_{\mathrm{F}}^{\mathrm{loss}}$). The resulting plot of d[F]/dt versus [F] in Fig. 4g–i clearly shows the bistability of [F].

Replacing the quantities [FG] and $\langle[\mathrm{FG}]\rangle_{\mathrm{cg}}$ by their steady-state functions $[\mathrm{FG}]^*$ and $\langle[\mathrm{FG}]\rangle^*_{\mathrm{cg}}$ results in the single-variable ODE for [F],

$$\frac{\mathrm{d}[\mathrm{F}]}{\mathrm{d}t} = \beta[\mathrm{G}] - \gamma[\mathrm{F}] + \alpha[\mathrm{FG}]^* - \phi p_{\mathrm{f}} N[\mathrm{G}]\langle[\mathrm{FG}]\rangle^*_{\mathrm{cg}}, \quad (10)$$

where $[\mathrm{FG}]^*$, $\langle[\mathrm{FG}]\rangle^*_{\mathrm{cg}}$ are functions of [F] and ϕ (as shown in Fig. 4a-c), and [G]=1−[F]. With these functions $[\mathrm{FG}]^*$ and $\langle[\mathrm{FG}]\rangle^*_{\mathrm{cg}}$, the observed bistability is caused by a classic double-well potential of the gradient system Eq. 10. In this ODE, nonlinearities emerge due to the equilibrium dependence of the interface on forest area (affecting $[\mathrm{FG}]^*$ and $\langle[\mathrm{FG}]\rangle^*_{\mathrm{cg}}$), due to the segmentation of grass cells near and below the percolation threshold (affecting $\langle[\mathrm{FG}]\rangle^*_{\mathrm{cg}}$) and due to dependence of the ignition rate on grass patch size (multiplying $\langle[\mathrm{FG}]\rangle^*_{\mathrm{cg}}$ with [G]). In Fig. S1, we show the roots of Eq. 10 using a nonparameteric fit of $[\mathrm{FG}]^*([\mathrm{F}];\phi)$ and $\langle[\mathrm{FG}]\rangle^*_{\mathrm{cg}}([\mathrm{F}];\phi)$. These match well with the steady states obtained via control (dot-dashed red).

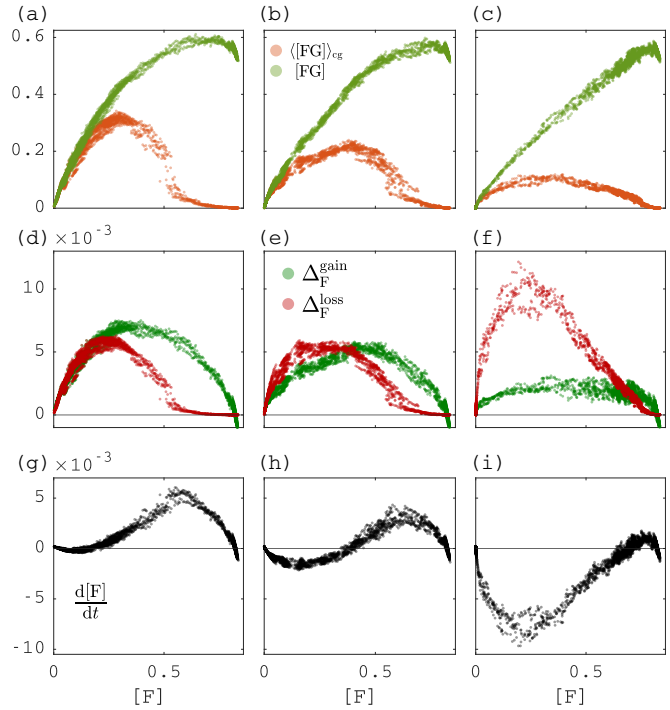

FIG. 4. Emergent relations between key quantities and forest area [F]: (a–c) forest perimeter [FG] and grassland-weighted forest perimeter $\langle[\mathrm{FG}]\rangle_{\mathrm{cg}}$, (d–f) forest gain terms and loss terms in Eqs. 5 and 8, (g–i) forest area rate of change (d/dt)[F] from Eq. 9. Columns correspond to vertical dashed lines in Fig. 2 (ϕN=0.257, ϕN=0.38, ϕN=1.32). Domain size: 100x100 cells.

If there is only one connected component of grass cells, we have $\langle[\mathrm{FG}]\rangle_{\mathrm{cg}}$=[FG], such that Eq. 10 simplifies to

$$\frac{\mathrm{d}[\mathrm{F}]}{\mathrm{d}t} = \beta[\mathrm{G}] - \gamma[\mathrm{F}] + (\alpha - \phi p_{\mathrm{f}} N[\mathrm{G}])[\mathrm{FG}]^*. \quad (11)$$

For homogeneous initial conditions (i.e. [F] is about the same in different large subsections of the domain), this approximation is expected to be valid for small [F], where most grass cells belong to the giant connected component (see Fig. S2). Figure S1 shows the resulting steady states of Eq. 11 as a function of ϕ and [F] when only using the fit of $[\mathrm{FG}]^*([\mathrm{F}];\phi)$ (dashed blue). The approximation is good for landscapes with low forest cover ([F] $\lesssim$ 0.2). Above [F] $\approx$ 0.2, it fails because the grassland breaks up into multiple clusters and fires are smaller than in case of a single cluster. Figure 4a–c already indicated that the single-cluster approximation is accurate for low forest cover since $\langle[\mathrm{FG}]\rangle_{\mathrm{cg}}\approx$[FG] for low [F] in the scatterplots.

Resilience to perturbations

One can evaluate the right-hand side of Eq. 9 for a landscape before and after application of a small perturbation, to determine if the perturbation will be dampened or amplified under the dynamics. More precisely,

we may define the sensitivity as

$$\lambda_{\mathrm{F}}(X,\delta X) := \frac{\Delta[\dot{\mathrm{F}}](X,\delta X)}{\Delta[\mathrm{F}](X,\delta X)} = \frac{[\dot{\mathrm{F}}](X+\delta X)-[\dot{\mathrm{F}}](X)}{[\mathrm{F}](X+\delta X)-[\mathrm{F}](X)}, \tag{12}$$

for a landscape X and a perturbation δX, where $[\dot{\mathrm{F}}]$ is the right-hand side of Eq. 9. Negative values of λ_{F} correspond to dampening (negative feedback) and positive values to amplification (positive feedback). Given that the dynamics of Eq. 9 are approximately scalar, the average of $\lambda_{\mathrm{F}}(X+\delta X)$ over naturally expected perturbations δX (call this $\bar{\lambda}_{\mathrm{F}}(X)$; see Methods, Eq. M9) can be interpreted as the approximate derivative $\mathrm{d}[\dot{\mathrm{F}}]([\mathrm{F}])/\mathrm{d}[\mathrm{F}]$, which fully characterises the local stability of the landscape. The scalar dynamics imply that Eq. 9 is a gradient system, such that $\bar{\lambda}_{\mathrm{F}}(X)$ is the concavity of the potential energy function at X, corresponding to the classic potential-well metaphor of local resilience [4, 5]. Figure 5d shows $\bar{\lambda}_{\mathrm{F}}(X)$ for the traversed landscapes when tipping up or down to the forest or grassland state (same landscapes as in Fig. 3b,d,f,g). This suggests that sign and magnitude of $\bar{\lambda}_{\mathrm{F}}(X)$ are indicators for the stability or criticality of a landscape. Comparison of the magnitude of $\bar{\lambda}_{\mathrm{F}}(X)$ in the alternative stable states reveals that (for parameters of Fig. 3d,f,g) the grassland state is more resilient than the forest state. Figure 5a–c shows the positive feedback for a forest landscape with a hole of critical size (same landscape as shown at t=0 in Fig. 3b). Panel b shows which cells along the perimeter of the largest grass cluster contribute to the loss term $\Delta_{\mathrm{F}}^{\mathrm{loss}}$ (red) and the gain term $\Delta_{\mathrm{F}}^{\mathrm{gain}}$ (green). Panel a shows the effect of the perturbation obtained by converting the green cells to forest, which causes an increase in $[\dot{\mathrm{F}}]$ (more green in panel a). Panel c shows the effect of the perturbation converting the red cells to grass, which causes a decrease in $[\dot{\mathrm{F}}]$ (more red in panel c), illustrating the spatial distribution of the positive feedback.

One could, in principle, also test the effect of large perturbations, and whether they will induce a transition to an alternative stable state, but it is not in general clear which perturbations are to be expected. However, in the special case of β=γ=0, when the large perturbation is a single hole in contiguous forest, only the size of the hole matters, and a simple expression for the critical size required to tip abruptly to a non-forest state can be derived (see Methods, Eq. M8).

Comparison to mean-field approximations

Our analysis of Eq. 9 enabled us to obtain macroscopic steady states and dynamics without making mean-field assumptions. Sections S3 and S4 derive a hierarchy of mean-field models for which we compare their predictions to our results to examine their validity. The simple mean field (Section S3) is unable to capture repeated fire extinction on a fast timescale and nearest-neighbour spreading of forest and fire, leading to severe bias. When instead assuming timescale separation between forest and fire dynamics and treating fire as a site percolation process in landscapes with uniform random placement of forest, we obtain the mean-field approximation of Eq. 9:

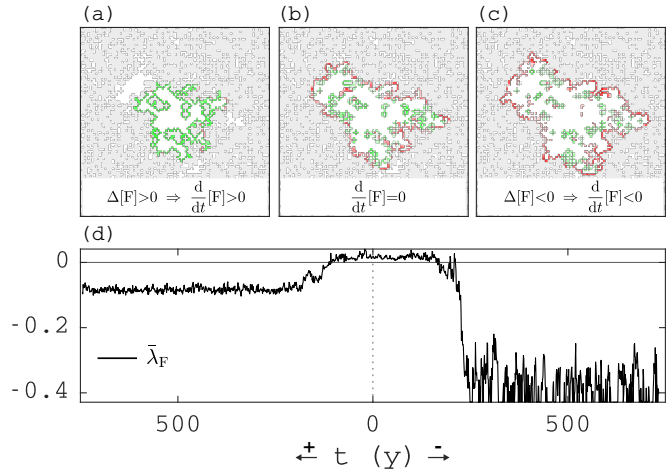

FIG. 5. Resilience of forest-grass landscape to perturbations. (a–c) Spatially resolved contributions to forest gain (green) and loss (red) rates at the forest perimeter of the largest grass cluster: (b) for the saddle solution (where $\Delta_{\mathrm{F}}^{\mathrm{gain}}\approx\Delta_{\mathrm{F}}^{\mathrm{loss}}$), (a) for a perturbation of the saddle with more forest at the perimeter (resulting in $\Delta_{\mathrm{F}}^{\mathrm{gain}}>\Delta_{\mathrm{F}}^{\mathrm{loss}}$), and (c) for a perturbation of the saddle with less forest at the perimeter (resulting in $\Delta_{\mathrm{F}}^{\mathrm{loss}}>\Delta_{\mathrm{F}}^{\mathrm{gain}}$). (d) Sensitivity to perturbations (Eq. 12) for all the traversed landscapes when tipping from the saddle: down to the grassland state (t^-), or, up to the forest state (t^+). The used landscapes correspond to the red vertical dashed line in Fig. 2 and the rightmost columns in Figs. 3 and 4.

$$\frac{\mathrm{d}}{\mathrm{d}t}[\mathrm{F}] = \beta[\mathrm{G}] + 4\alpha[\mathrm{F}][\mathrm{G}] - \gamma[\mathrm{F}] - \phi N p_{\mathrm{f}}[\mathrm{G}]\langle[\mathrm{FG}]\rangle_{\mathrm{cg}}^{\mathrm{u}}. \tag{13}$$

In Eq. 13 we substituted the a-priori unknown forest perimeter [FG] and the grassland-weighted perimeter $\langle[\mathrm{FG}]\rangle_{\mathrm{cg}}$ by their expressions assuming uniform random (i.e., spatially uncorrelated) placement of forest: $[\mathrm{FG}]\approx 4[\mathrm{F}][\mathrm{G}]$ and $\langle[\mathrm{FG}]\rangle_{\mathrm{cg}}\approx\langle[\mathrm{FG}]\rangle_{\mathrm{cg}}^{\mathrm{u}}$ for given [F]. The function $\langle[\mathrm{FG}]\rangle_{\mathrm{cg}}^{\mathrm{u}}([\mathrm{F}])$ is given by Eq. 7 and plotted in Fig. S3a–c (orange). Eq. 13 is bistable with stable high and low forest cover steady states over a wide range of parameters. It accurately predicts the location of both stable steady states (blue line in Fig. S4). Yet, its prediction of the threshold (unstable) steady state and the dynamics remains strongly biased. Indeed, away from the stable steady states, the interplay of forest demography and fire-induced forest erosion creates landscapes in which forest is spatially aggregated, strongly violating the assumption of absence of correlations. This can be seen in Fig. S3a–c, which shows that for given forest area [F], the forest perimeter of simulations, [FG], lies below that predicted by the mean-field, $[\mathrm{FG}]_{\mathrm{mf}}$, i.e.

$$[\mathrm{FG}] < [\mathrm{FG}]_{\mathrm{mf}} = 4[\mathrm{F}](1-[\mathrm{F}]), \tag{14}$$

implying that forest is more spatially aggregated than assumed in the mean field. Aggregation results from forest spreading close to existing forest and from lower survival of forest cells that are more exposed to fire (i.e., less aggregated). Forest gain is smaller when aggregated (Fig. S3 d–f) due to the smaller perimeter. Forest loss is smaller at low cover while it is larger at high forest cover compared to uniform random landscapes (Fig. S3 d–f). This is so because aggregation makes forest cells individually less exposed to fire, but collectively less effective at blocking fires, where the individual effect is dominant at low cover and the collective effect is dominant at cover values near and above the fire percolation threshold.

For our choice of parameters, the stable steady states and the lower saddle-node bifurcation contain negligible spatial structure, such that mean-field predictions are accurate. We derive their expressions below for $\beta\approx 0$.

Stable steady states By Eq. 13, the low-cover steady state $[\mathrm{F}]^*_-$ has to be approximately zero for $\beta\approx 0$. At high forest cover, loss due to fire is negligible, such that the high-cover steady state $[\mathrm{F}]^*_+$ can also be obtained from Eq. 13 (using $\beta\approx 0$):

$$[\mathrm{F}]^*_- = 0, \qquad [\mathrm{F}]^*_+ = 1 - \frac{\gamma}{4\alpha}. \tag{15}$$

For the chosen parameters, we have $[\mathrm{F}]^*_+=0.83$, which is in excellent agreement with simulations (Fig. 2).

* Onset of bistability At low forest cover, grass consists of a single cluster, such that we can write in Eq. 13 $\langle[\mathrm{FG}]\rangle^{\mathrm{u}}_{\mathrm{cg}}=[\mathrm{FG}]=4[\mathrm{F}][\mathrm{G}]$. Hence (when $\beta\approx 0$):

$$\frac{\mathrm{d}}{\mathrm{d}t}[\mathrm{F}] = 4\alpha[\mathrm{F}][\mathrm{G}] - \gamma[\mathrm{F}] - 4\phi N p_{\mathrm{f}}[\mathrm{G}]^2[\mathrm{F}]. \tag{16}$$

An expression for the lower bifurcation point can be obtained by finding the root of the derivative of the right-hand side of Eq. 16 with respect to [F] at $[\mathrm{F}]=[\mathrm{F}]^*_-=0$, giving the relation $4\alpha - \gamma - 4\phi N p_{\mathrm{f}} = 0$. Rearranging this relation for ϕN, we can obtain the fire ignition rate above which tropical forests are bistable with grasslands:

$$(\phi N)_{\min} = \frac{1}{p_{\mathrm{f}}}(\alpha - \frac{\gamma}{4}). \tag{17}$$

For the chosen parameters, $(\phi N)_{\min}=0.25$, which agrees well with simulations (Fig. 2) and which corresponds to a maximum fire return interval of $(\phi N)^{-1}_{\min}=4$y.

DISCUSSION

In this paper, we examined the spatial structure and dynamics that emerge from the microscopic rules of fire and forest spread in the tropics, and their consequences for bistability and resilience. Relying on the microscopic simulation model of forest and fire spread proposed by [12], we derived a macroscopic balance equation for forest area change that respects the emerging spatial structure (Eq. 9). Instead of using mean-field assumptions, we started from the observation that fire spreads on grass much faster than forest and assumed that it spreads perfectly, reaching the entire perimeter of the ignited grass patch, and damaging the forest at this perimeter. This made two macroscopic quantities relevant as separate terms in Eq. 9: the forest perimeter [FG] for gain from forest spread, and, the grassland-weighted forest perimeter $\langle[\mathrm{FG}]\rangle_{\mathrm{cg}}$ for loss induced by fire. Simulations initiated at the unstable steady states enabled us to explore the whole phase space and revealed that these quantities are evolving on a much faster timescale than forest area, such that on the slow timescale and for given parameters, they are equilibrium functions of forest area. When replacing the perimeter quantities with their steady state functions of forest area, Eq. 9 reduces to a one-variable ODE (Eq. 10). In this emergent relation between forest change and forest area, nonlinear terms arise due to interactions at the forest-grass interface whereas linear terms arise from spontaneous transitions occurring anywhere in space. This shows that a closed macroscopic evolution equation exists, but that, due to processes at the forest perimeter, it is generally very different from the mean-field approximation. Similar to mean-field models in previous work [9, 20–22], Eq. 10 does not include fire explicitly, as it does not contain equations for fire. Instead, it accounts for the effect of fire by exploiting its relation with the steady-state landscape structure. This follows from timescale separation between fire and vegetation dynamics, an assumption (see (*i*) in the Introduction) that was already implicit in mean-field models [9, 20–22] and microscopic models [10, 11] focusing on alternative stable states. However, by assuming well-mixedness (see (*ii*), Introduction) in all interactions (mean-field models) or in the interaction of tree patches and fire (microscopic models), previous models failed to account for the steady-state landscape structure emerging from the interplay of fire and vegetation dynamics.

In the rest of our discussion, we evaluate mean-field models in light of our results, illustrate the role of finite-size effects in bistability, and consider the relevance of our results for resilience assessment and conservation.

Evaluation of mean-field models The feedback control (see Methods) enabled us to compare the simulated dynamics to mean-field approximations over the whole range of [F] and for any choice of parameters. This showed that mean-field models are in qualitative but not quantitative agreement with simulations: existence of bistability, but not its parameter range is robust to mixing assumptions. In particular, the simple mean field (Eq. S7) is strongly biased due to its failure to account for two phenomena that are present in the microscale model: (*i*) spontaneous fire extinction on the fast timescale, leading to separated rapid fire spreading events, (*ii*) nearest-neighbour spreading of fire and forest, leading to emergent aggregation of forest patches away from the steady states. The former violates the mean-field assumption of large system size ($N\to\infty$) and the latter that of well-mixedness. That spatial structure changes the dynam-

ics compared to the well-mixed case is well known [e.g. 23, 24]. Even when addressing timescale separation and using results from percolation theory for the effect of fire (Eq. S18 or Eq. S22), a large bias remains except near the alternative stable states (see Fig. S3). This is because standard percolation theory only considers lattice configurations with uniform random placement of flammable sites while our forest-grass landscapes are shaped by past fires and vegetation dynamics. As Fig. 3a,b (at t=0) shows, aggregation of forest is particularly strong at the tipping threshold for forest collapse, implying that mean-field models cannot be used to study abrupt forest dieback. Despite their generally severe bias concerning forest dynamics and tipping, mean-field models are still useful for studying well-mixed regimes, such as near the stable equilibria or for dynamics with uniform seed dispersal. This enabled us to derive expressions for these equilibria (Eq. 15) and the point of onset of bistability (Eq. 17). The latter result was not obtained by previous mean-field models because they did not include parameters that relate directly to fire [9, 10, see Section S6 for a suggested modification] or they did not account for timescale separation in finite domains [12].

Finite sizes and bistability In simple bistable chemical systems, it is known that bistability converges to an abrupt phase transition in the thermodynamic limit ($N\to\infty$) [30, 31], at a value known as the Maxwell point [e.g. 32], making the macroscopic state of the system deterministically dependent on the parameters (e.g. pressure or temperature). With only forest and grass or provided that savanna and forest components are sufficiently decoupled, the same behaviour occurs in spatial mean-field models of tropical forest, with a front between forest and nonforest that is depends deterministically on environmental drivers [21]. We do not expect such determinism as $N\to\infty$ to arise in the FGBA cellular automaton. The infinite FGBA cellular automaton possesses grass clusters of arbitrary size, such that, even when assuming that fire spreads instantly on grass, there will always be some parts of the forest perimeter shielded from intruding fires by adjacent ash cells. Were it not for this shielding effect, then there would be a deterministic dependence of the dynamics on fire ignition rate away from the absorbing states: ϕ=0 would lead to forest spread while ϕ>0 would lead to forest extinction (see Section S5, for β=γ=0). In reality, finite fire spreading rates and, in particular, the effects of heterogeneity in space or time impose stronger limits on the reach of fires. Hence, while, due to the large size of a typical system of molecules, the thermodynamic limit is usually of practical relevance in context of materials, in case of ecosystems, finite sizes and their effects are the norm. In finite domains, both the cellular automaton and scalar reaction-diffusion equations show bistability due to critical patch sizes and dependence on interfacial characteristics [e.g. 22, 33], but this correspondence requires further scrutiny. In realistic scenarios, the amount of bistability then depends (besides the parameters) on a 'characteristic system size', which in turn depends on e.g. fire spreading and/or plant dispersal ranges. How this is affected by environmental heterogeneity is subject of future work.

Implications for resilience assessment and conservation The ability to analyse bistability and resilience in terms of landscape structure and measurable parameters tied to the underlying processes instead of statistical properties of spatial vegetation data (such as bimodality) enables researchers to avoid the problems of spatial heterogeneity and of lack of attribution to underlying processes. The parameters of the microscopic reaction rules (given in Table M1) can be inferred from remote-sensed data [as in 12] or from experiments [as for fire spread in 19]. From these parameters, one can directly obtain the minimum fire ignition rate for onset of bistability (Eq. 17), which was derived from the mean field, and, which is hence accurate if the steady states contain negligible spatial structure. This expression can show which natural or abandoned degraded areas of low tree cover with fire ignition rate beyond this point will not spontaneously recover to closed tropical forest. Away from the stable equilibria, the mean field is highly inaccurate (Fig. S3). In particular, the tipping threshold becomes spatially structured at higher fire ignition rate (Fig. 3a,b at t=0) and approaches the stable forest equilibrium much more closely than in the mean field (Fig. S4). While this makes the mean field unsuitable for studying forest resilience and dieback, our balance equation (Eq. 9) does not have this limitation because it does not assume well-mixedness. Even though Eq. 9 is not a closed equation, one can evaluate its right-hand side for any given landscape by calculating the perimeter quantities $[\mathrm{FG}]$ and $\langle[\mathrm{FG}]\rangle_{\mathrm{cg}}$ (and forest cover $[\mathrm{F}]$). Equation 9 further permits, via λ_{F} (Eq. 12), estimation of the resilience of a landscape to perturbations. In contrast to generic indicators of resilience [4, 34], λ_{F} is an indicator that can be obtained from a single landscape, and for which the contribution of each relevant spatial process can be examined. Furthermore, landscape perturbations by human intervention can be evaluated through sensitivity λ_{F} for how they will amplify or mitigate fire-vegetation feedback. Forest conservation/restoration may introduce targeted perturbations that most efficiently prevent resilience loss of high-cover states or induce resilience loss of low-cover states. For instance, in Fig. 5a, forest dieback is averted by a perturbation that divides the largest grass cluster into smaller ones. It may thus be anticipated that maintenance or creation of barriers to fire spread will be essential here.

Further realism, such as environmental heterogeneity, longer dispersal ranges, density-dependent mortality, presence and dynamics of other tree types and life stages [such as in savanna dynamics: 9–11, 20, 35–40], or vegetation-rainfall feedback [41], will modify Eq. 9. This may result in additional relevant quantities and dependence on more variables than only forest area. Our approach is applicable to any spatiotemporal complex sys-

tem with timescale separation, and should thus extend to other applications in spatial ecology and beyond.

METHODS

Details of the FGBA probabilistic cellular automaton The FGBA probabilistic cellular automaton is a minimal spatial stochastic process that models the joint dynamics of tropical vegetation and fire. It is an adapted version of the BGT(A) model of ref. [12]. The modifications compared to ref. [12] are: (*i*) it runs in continuous time, (*ii*) it includes a spontaneous forest mortality rate γ, (*iii*) species T is labelled as F, consistent with other models of tropical vegetation dynamics [9, 11, 21]. Note that according to some definitions, probabilistic continuous-time cellular automata are considered as interacting particle systems. In general, when studying the stochastic dynamics of a number n of interacting species on a square lattice with N cells, the state of the system can be represented as

$$X := (X_1, X_2, ..., X_N),$$

where X_i is the label of the species that occupies cell i. Each cell is occupied by exactly one of four possible species: grass, forest, burning and ash, with labels G, F, B and A. Transitions between states (species) occur in continuous time, resulting in a continuous-time Markov chain with a state space of size n^N. The reaction rules for transitions between states are shown in Table M1, where spontaneous conversions are shown on the left and conversions due to nearest-neighbour interactions on the right (see also Fig. 1a).

TABLE M1. Reactions and rates (y^{-1}) in the FGBA cellular automaton.

	Spontaneous	Spread
forest	$\mathrm{G,A} \xrightarrow{\beta} \mathrm{F}, \quad \beta = 2\cdot 10^{-4}$	$\mathrm{GF,AF} \xrightarrow{\alpha} \mathrm{FF}, \quad \alpha = 3\cdot 10^{-2}$
	$\mathrm{F} \xrightarrow{\gamma} \mathrm{G}, \quad \gamma = 2\cdot 10^{-2}$	
fire	$\mathrm{G} \xrightarrow{\phi} \mathrm{B}, \quad \phi = [0,2]\cdot 10^{-4}$	$\mathrm{GB} \xrightarrow{\rho_\mathrm{g}} \mathrm{BB}, \quad \rho_\mathrm{g} = 9\cdot 10^{6}$
	$\mathrm{B} \xrightarrow{\mu} \mathrm{A}, \quad \mu = 10^{6}$	$\mathrm{FB} \xrightarrow{\rho_\mathrm{f}} \mathrm{BB}, \quad \rho_\mathrm{f} = 1.11\cdot 10^{5}$
	$\mathrm{A} \xrightarrow{\lambda} \mathrm{G}, \quad \lambda = 5$	

The latter type of interaction occurs over each four nearest neighbour connections of the indicated type. E.g., fire will spread into a given grass cell with a rate ρ_g for each burning neighbour. For realistic timescales, our parameters satisfy Eqs. 1 and 2, which were empirically justified in [12]. We borrow our notation from the moment closure literature [e.g. 23, 24, 42, 43], writing the global fraction of species with label x and the interface between species with label x with label y respectively as

$$[\mathrm{x}] := \frac{1}{N}\sum_i^N \delta_\mathrm{x}(X_i), \quad [\mathrm{xy}] := \frac{1}{N}\sum_{i,j}^N \mathsf{A}_{ij}\delta_\mathrm{x}(X_i)\delta_\mathrm{y}(X_j), \tag{M1}$$

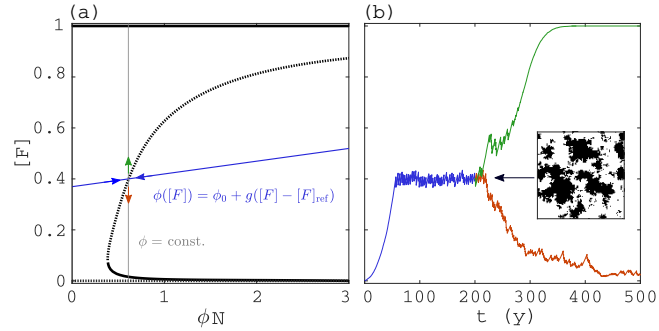

FIG. M1. Feedback control applied to the cellular automaton without spontaneous mortality (γ=0): (a) the unstable steady state of the bifurcation diagram (dashed) was derived via feedback control by letting ϕ be a function of [F] (blue line) such that it is stabilised, then obtaining (ϕ, [F]) by averaging and repeating this for many $[\mathrm{F}]_\mathrm{ref}$ (with appropriate g), (b) a regular simulation with the same ϕ value (solid grey in (a)) and starting from the final state of the controlled simulation tips up or down depending on initial perturbations, (c) snapshot of the domain at the saddle for the control indicated in (a) (black: forest, white: grass). For other parameters, see Table M1.

where both are normalised by N, δ is the Kronecker delta function ($\delta_\mathrm{x}(y)$=1 if y=x and 0 otherwise) and $\mathsf{A} \in \{0,1\}^{N\times N}$ the adjacency matrix. We simulated the cellular automaton via a Gillespie algorithm [44] and used a domain of N=100×100 (N=200×200 in Fig. 1) cells with periodic boundary conditions.

Noninvasive feedback control To study steady states regardless of their stability in a simulation, we apply noninvasive feedback control [45–48]. To obtain the dependence of equilibria of [F] on fire ignition rate ϕ, we introduced an artificial stabilizing feedback loop of the form

$$\phi(t) = \phi_0 + g([\mathrm{F}](t) - [\mathrm{F}]_\mathrm{ref}). \tag{M2}$$

The factor g is called the feedback control gain and is problem specific. The property of noninvasiveness means that the controlled simulations have the same equilibria as regular simulations [49–51]. This implies that if one extracts the equilibrium values of the controlled simulation (ϕ^*, $[\mathrm{F}]^*$), one can use them to plot a 1-parameter bifurcation diagram of the simulation without control.

Figure M1 shows the control graphically. The feedback Eq. M2, indicated in blue in Fig. M1a, stabilises a steady state that is unstable in a regular simulation. This can be seen in Fig. M1b, where the unstable steady state is first stabilised via control, after which the control is removed and a regular simulation is started with the effective rate and the landscape (inset) obtained from the controlled simulation. Depending on initial perturbations, the regular simulation gets either attracted to the 100% forest state or to the low tree cover state. When the controlled simulation is in equilibrium (steady part of the blue curve in Fig. M1b), the steady state values of [F] are obtained

via taking the time average, i.e.

$$\overline{[\mathrm{F}]} = \frac{1}{T}\int_{t_0}^{t_0+T} [\mathrm{F}](t)dt, \tag{M3}$$

where t_0 is the time after which the dynamics have settled to a steady state and T the averaging time. If $n_{\mathrm{G}\to\mathrm{B}}$ is the number of ignition events between $t = t_0$ and $t = t_0 + T$, the steady state of ϕ is obtained by calculating the mean ignition rate as $n_{\mathrm{G}\to\mathrm{B}}/T$ and dividing this by the mean number of grass cells, such that

$$\bar{\phi} = \frac{n_{\mathrm{G}\to\mathrm{B}}/T}{\overline{[\mathrm{G}]}}, \tag{M4}$$

where $\overline{[\mathrm{G}]}$ is obtained as in Eq. M3. When repeating this exercise for many $[\mathrm{F}]_{\mathrm{ref}}$ values, one can get multiple points on the unstable branch. Points on the stable branches can be obtained with regular simulations. On the final selection of points, we applied Gaussian process regression to obtain smooth curves and used moving block bootstrapping [52] to obtain confidence intervals. One of the advantages of applying control is that one can obtain states for which one would have to wait prohibitively long in a regular simulation due to their instability.

Forest loss due to a single fire A fire in grassland cluster with index j that reaches its interface with adjacent forest induces a forest loss that can be approximated as follows. Consider a single forest cell i located at the interface with grassland cluster j with $[\mathrm{FG}]_{i,j}$ number of neighbouring grass cells. When assuming that spreading events are independent, the probability that the forest cell gets burnt is the complement of the probability that none of its neighbouring grass cells in cluster j spread the fire to the forest cell:

$$q_{i,j} := 1 - (1 - p_{\mathrm{f}})^{[\mathrm{FG}]_{i,j}} \approx p_{\mathrm{f}}[\mathrm{FG}]_{i,j}, \tag{M5}$$

where the approximation on the right is valid for small p_{f}. Summing over all forest cells at the interface of grassland cluster j, we obtain the expected loss of forest per fire event as shown in Eq. 4:

$$\Delta^{\mathrm{loss}}_{\mathrm{F},j} := \sum_i q_{i,j} = p_{\mathrm{f}}[\mathrm{FG}]_j. \tag{M6}$$

This approximation also assumes that burning forest cells at the interface do not spread the fire further, which also relies on p_{f} being small. For an evaluation of the validity of this approximation in case of well-mixed landscapes, see Fig. S8.

Critical hole size for an abrupt shift when γ=β=0 When there are no spontaneous transitions and we perturb a fully closed forest of 100% cover by creating a hole with grassland, an expression can be obtained for the critical hole size beyond which fire causes an abrupt shift to grassland. Using that grassland is a single cluster, Eq. 9 becomes

$$\frac{\mathrm{d}[\mathrm{F}]}{\mathrm{d}t} = (\alpha - \phi N p_{\mathrm{f}}[\mathrm{G}])[\mathrm{FG}], \tag{M7}$$

which has two absorbing steady states $[\mathrm{F}]^*_{\mathrm{l}}$=0 and $[\mathrm{F}]^*_{\mathrm{h}}$=1, and an unstable steady state at $[\mathrm{F}]^*_{\mathrm{c}}$=$1 - \frac{\alpha}{\phi N p_{\mathrm{f}}}$. The critical hole size is then the complement of the unstable steady state:

$$[\mathrm{G}]_{\mathrm{c}} = \frac{\alpha}{\phi N p_{\mathrm{f}}}, \tag{M8}$$

which can also be written as $[\mathrm{G}]_{\mathrm{c}} = \phi_1/\phi$, where ϕ_1 is the value of ϕ for which $[\mathrm{G}]_{\mathrm{c}} = 1$, or also the lower limit of the bistablity range.

Sensitivity to perturbations We estimated $\bar{\lambda}_{\mathrm{F}}$ in Fig. 5d for a given landscape by averaging Eq. 12 over realisations of different types of perturbations:

$$\bar{\lambda}_{\mathrm{F}} = \langle \frac{\sum_i w_i \Delta[\dot{\mathrm{F}}](X, (\delta X)_i)}{\sum_i w_i \Delta[\mathrm{F}](X, (\delta X)_i)} \rangle. \tag{M9}$$

Each of $(\delta X)_i$ are perturbations that one might expect in simulations, such as removal of a fraction of perimeter forest cells in the largest grass cluster or spontaneous mortality/growth of forest. The weights w_i are determined by the rates/probabilities of occurrence of the perturbations. The $\langle\cdot\rangle$ denote an average over 64 realisations.

ACKNOWLEDGEMENTS

This work was supported by the UK EPSRC (grants EP/N023544/1 and EP/V04687X/1) and the EU Horizon 2020 TiPES project (grant 820970, output no. 171).

[1] A. C. Staver, S. Archibald, and S. A. Levin, Science **334**, 230 (2011).
[2] M. Hirota, M. Holmgren, E. H. Van Nes, and M. Scheffer, Science **334**, 232 (2011).
[3] T. M. Lenton, H. Held, E. Kriegler, J. W. Hall, W. Lucht, S. Rahmstorf, and H. J. Schellnhuber, Proceedings of the National Academy of Sciences **105**, 1786 (2008).
[4] M. Scheffer, J. Bascompte, W. A. Brock, V. Brovkin, S. R. Carpenter, V. Dakos, H. Held, E. H. van Nes, M. Rietkerk, and G. Sugihara, Nature **461**, 53 (2009), arXiv:arXiv:1011.1669v3.
[5] M. Scheffer, S. R. Carpenter, V. Dakos, and E. H. Van Nes, Annual Review of Ecology, Evolution, and Systematics **46**, 145 (2015).
[6] B. Wuyts, A. R. Champneys, and J. I. House, Nature Communications **8**, 15519 (2017).
[7] N. P. Hanan, A. T. Tredennick, L. Prihodko, G. Bucini, and J. Dohn, Global Ecology and Biogeography **23**, 259

(2014).
[8] F. Gerard, D. Hooftman, F. van Langevelde, E. Veenendaal, S. M. White, and J. Lloyd, Global Ecology and Biogeography **26**, 854 (2017).
[9] A. C. Staver and S. A. Levin, The American Naturalist **180**, 211 (2012).
[10] E. Schertzer, A. C. Staver, and S. A. Levin, Journal of Mathematical Biology **70**, 329 (2015).
[11] D. D. Patterson, S. A. Levin, C. Staver, and J. D. Touboul, SIAM Journal on Applied Dynamical Systems **19**, 2682 (2021).
[12] L. Hébert-Dufresne, A. F. Pellegrini, U. Bhat, S. Redner, S. W. Pacala, and A. M. Berdahl, Ecology Letters **21**, 794 (2018).
[13] W. J. Bond, Annual Review of Ecology, Evolution, and Systematics **39**, 641 (2008).
[14] W. A. Hoffmann, E. L. Geiger, S. G. Gotsch, D. R. Rossatto, L. C. Silva, O. L. Lau, M. Haridasan, and A. C. Franco, Ecology Letters **15**, 759 (2012).
[15] S. Archibald, D. P. Roy, B. W. van Wilgen, and R. J. Scholes, Global Change Biology **15**, 613 (2009).
[16] E. H. Van Nes, A. Staal, S. Hantson, M. Holmgren, S. Pueyo, R. E. Bernardi, B. M. Flores, C. Xu, and M. Scheffer, PloS One **13**, e0191027 (2018).
[17] D. Stauffer and A. Aharony, *Introduction to percolation theory* (CRC press, 1994).
[18] K. Christensen and N. R. Moloney, *Complexity and Criticality*, Imperial College Press Advanced Physics Texts, Vol. 1 (Imperial College Press and Distributed, 2005).
[19] A. W. Cardoso, S. Archibald, W. J. Bond, C. Coetsee, M. Forrest, N. Govender, D. Lehmann, L. Makaga, N. Mpanza, J. E. Ndong, A. F. Koumba Pambo, T. Strydom, D. Tilman, P. D. Wragg, and A. C. Staver, Proceedings of the National Academy of Sciences of the United States of America **119** (2022), 10.1073/pnas.2110364119.
[20] J. D. Touboul, A. C. Staver, and S. A. Levin, Proceedings of the National Academy of Sciences , 201712356 (2018).
[21] B. Wuyts, A. R. Champneys, N. Verschueren, and J. I. House, PLoS ONE **14**, e0218151 (2019).
[22] N. Goel, V. Guttal, S. A. Levin, and A. C. Staver, American Naturalist **195**, 833 (2020).
[23] M. J. Keeling, Proceedings of the Royal Society B: Biological Sciences **266**, 859 (1999).
[24] U. Dieckmann, R. Law, and J. A. J. Metz, *The geometry of ecological interactions : simplifying spatial complexity* (Cambridge University Press, 2000) p. 564.
[25] A. L. Sullivan, International Journal of Wildland Fire **18**, 387 (2009).
[26] J. C. Menaut, J. Gignoux, C. Prado, and J. Clobert, Journal of Biogeography **17**, 471 (1990).
[27] M. E. Hochberg, J. C. Menaut, and J. Gignoux, The Journal of Ecology **82**, 217 (1994).
[28] C. Favier, J. Chave, A. Fabing, D. Schwartz, and M. A. Dubois, Ecological Modelling **171**, 85 (2004).
[29] A. Staal, E. H. van Nes, S. Hantson, M. Holmgren, S. C. Dekker, S. Pueyo, C. Xu, and M. Scheffer, Global Change Biology **24**, 5096 (2018).
[30] H. Ge and H. Qian, Physical Review Letters **103**, 148103 (2009).
[31] U. Thiele, T. Frohoff-Hülsmann, S. Engelnkemper, E. Knobloch, and A. J. Archer, New Journal of Physics **21**, 123021 (2019), arXiv:1908.11304.
[32] N. Goldenfeld, *Lectures on Phase Transitions and the Renormalization Group* (CRC Press, 2018) pp. 1–394.
[33] A. Liehr, *Dissipative solitons in reaction diffusion systems*, Vol. 70 (Springer, 2013).
[34] C. A. Boulton, T. M. Lenton, and N. Boers, Nature Climate Change **12**, 271 (2022).
[35] F. Van Langevelde, C. A. Van De Vijver, L. Kumar, J. Van De Koppel, N. De Ridder, J. Van Andel, A. K. Skidmore, J. W. Hearne, L. Stroosnijder, W. J. Bond, H. H. Prins, and M. Rietkerk, Ecology **84**, 337 (2003).
[36] F. Accatino, C. De Michele, R. Vezzoli, D. Donzelli, and R. J. Scholes, Journal of Theoretical Biology **267**, 235 (2010).
[37] P. D'Odorico, F. Laio, and L. Ridolfi, The American naturalist **167** (2006), 10.1086/500617.
[38] M. Baudena, F. D'Andrea, and A. Provenzale, Journal of Ecology **98**, 74 (2010).
[39] B. Beckage, L. J. Gross, and W. J. Platt, Ecological Modelling **222**, 2227 (2011).
[40] A. Hoyer-Leitzel and S. Iams, Bulletin of Mathematical Biology **83** (2021), 10.1007/s11538-021-00944-x.
[41] D. V. Spracklen, J. C. Baker, L. Garcia-Carreras, and J. H. Marsham, "The effects of tropical vegetation on rainfall," (2018).
[42] I. Z. Kiss, J. C. Miller, and P. L. Simon, *Interdisciplinary Applied Mathematics*, Interdisciplinary Applied Mathematics, Vol. 46 (Springer International Publishing, Cham, 2017) pp. 1–413.
[43] B. Wuyts and J. Sieber, Physical Review E **106**, 054312 (2022), arXiv:2111.07643.
[44] D. T. Gillespie, Annual Review of Physical Chemistry **58**, 35 (2007).
[45] J. Sieber, A. Gonzalez-Buelga, S. A. Neild, D. J. Wagg, and B. Krauskopf, Phys. Rev. Lett. **100**, 244101 (2008).
[46] F. Schilder, E. Bureau, I. F. Santos, J. J. Thomsen, and J. Starke, Journal of Sound and Vibration **358**, 251 (2015).
[47] D. Barton, Mechanical Systems and Signal Processing **84**, 54 (2017).
[48] R. M. Neville, R. M. Groh, A. Pirrera, and M. Schenk, Physical review letters **120**, 254101 (2018).
[49] D. A. W. Barton and J. Sieber, Phys. Rev. E **87**, 052916 (2013).
[50] J. Sieber, O. E. Omel'chenko, and M. Wolfrum, Phys. Rev. Lett. **112**, 054102 (2014).
[51] L. Renson, D. Barton, and S. Neild, International Journal of Bifurcation and Chaos **27**, 1730002 (2017).
[52] J. P. Kreiss and S. N. Lahiri, in *Handbook of Statistics*, Vol. 30 (2012) pp. 3–26.
[53] Y. Y. Tarasevich and S. C. Van Der Marck, International Journal of Modern Physics C **10**, 1193 (1999).
[54] T. Tomé and M. J. De Oliveira, *Stochastic dynamics and irreversibility* (Springer, 2015) p. 394.
[55] R. Durrett, in *Epidemic models : their structure and relation to data* (New York, NY, 1995) pp. 187–201.
[56] T. Tomé and R. M. Ziff, Physical Review E - Statistical, Nonlinear, and Soft Matter Physics **82**, 051921 (2010).
[57] F. Crameri, "Scientific colour maps," (2018), `http://doi.org/10.5281/zenodo.1243862`.
[58] L. Hébert-Dufresne and A. Allard, Physical Review Research **1**, 13009 (2019), arXiv:1810.00735.

Supplement

S1. SUPPLEMENTARY FIGURES REFERENCED FROM THE MAIN TEXT

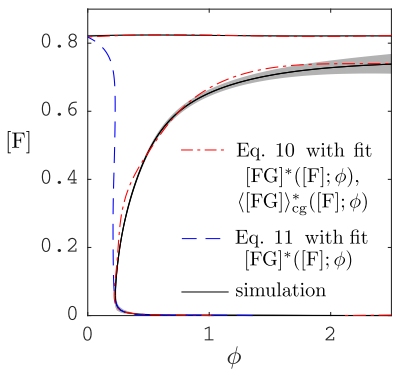

FIG. S1. Steady states of Eq. 10 (multicluster – dot-dashed red) and of Eq. 11 (single cluster – dashed blue) compared to controlled simulations (solid black with shading indicating two-standard deviation confidence interval of the mean). Parameters in the cellular automaton: γ=0.02, α=0.03, β=$2\cdot10^{-4}$, ρ_g=$9\cdot10^6$, ρ_f=$1.11\cdot10^5$, μ=10^6, λ=5.

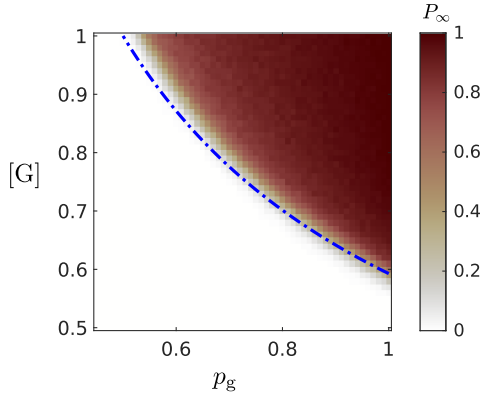

FIG. S2. Expected fraction of grass cells belonging to the giant connected component for uniformly randomly placed perfectly fire-blocking forest. Blue dashed-dotted curve is the theoretical prediction for the large-N limit for mixed percolation from [53]. The small bias occurs due to autocorrelations in connectivity between grass pairs as a consequence of spreading dynamics. See Section S2C and Fig. S12 for background and more detail.

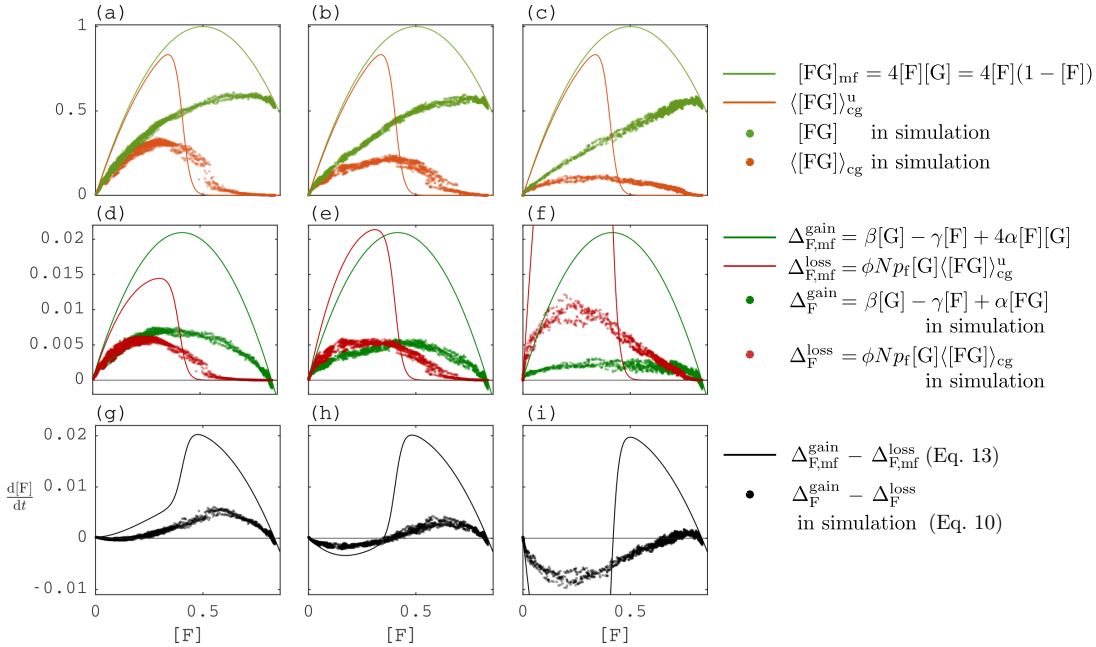

FIG. S3. Emergent relations between key quantities and forest area [F] compared to the mean field with site percolation (dots: simulations, lines: corresponding mean field quantities from Section S4B): (a–c) forest perimeter [FG] (green) and grassland-weighted forest perimeter $\langle[FG]\rangle_{cg}$ (orange), where green line equals 4[F][G] and orange line was called $\langle[FG]\rangle^u_{cg}$ in the main article, (d–f) forest gain terms and loss terms in Eqs. 5 and 6, (g–i) forest area rate of change (d/dt)[F] from Eq. 9. Columns correspond to vertical dashed lines in Fig. 2 (ϕN=0.257, ϕN=0.38, ϕN=1.32). Simulation results are identical to Fig. 4. Domain size: N=100x100 cells. See Section S4B for details of derivation for $\langle[FG]\rangle^u_{cg}$ and $[FG]_{mf}$.

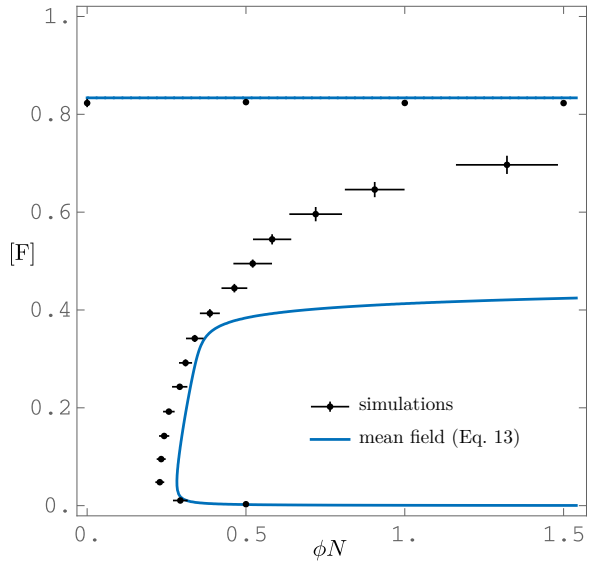

FIG. S4. Comparison of steady state forest as a function of ignition rate in the time-separated mean-field and in simulations (dots with error bars: simulations, lines: mean field). A large difference between mean-field model and simulation occurs for the threshold steady state, while the mean-field model is accurate for high- and low-tree-cover alternative stable states. See Section S4B and Fig. S10 for comparison of other scenarios and mean-field approximations.

S2. RELEVANT CHARACTERISTICS OF THE FIRE SPREADING PROCESS

Before obtaining the mean-field equations for coupled vegetation and fire dynamics, we analyse the fire spreading process in isolation. The insights from this section will enable us to set up a mean-field model that constitutes the fairest comparison against the analysis in the main text.

A. Definition and mean field

When we remove state F and its conversion rates to/from other types $(\alpha, \beta, \gamma, \rho_\mathrm{f})$ from the FGBA process, the dynamics show fire spread alone. We call this the *GBA process*. Writing x_i as shorthand for $\delta_\mathrm{x}(X_i)$ (equalling 1 if $X_i = \mathrm{x}$ and 0 otherwise) and taking expectations in each cell i, we obtain equations for the rate of change of the expectation that cell i is occupied by species $x \in \{\mathrm{G}, \mathrm{B}, \mathrm{A}\}$,

$$\begin{aligned}
\frac{\mathrm{d}}{\mathrm{d}t}\langle \mathrm{G}_i\rangle &= \lambda\langle \mathrm{A}_i\rangle - \big\langle \mathrm{G}_i(\phi + \textstyle\sum_{j\in\mathcal{N}(i)} \rho_\mathrm{g}\mathrm{B}_j)\big\rangle, \\
\frac{\mathrm{d}}{\mathrm{d}t}\langle \mathrm{B}_i\rangle &= \phi\langle \mathrm{G}_i\rangle - \mu\langle \mathrm{B}_i\rangle + \big\langle \rho_\mathrm{g}\mathrm{G}_i \textstyle\sum_{j\in\mathcal{N}(i)} \mathrm{B}_j\big\rangle, \\
\frac{\mathrm{d}}{\mathrm{d}t}\langle \mathrm{A}_i\rangle &= -\tfrac{\mathrm{d}}{\mathrm{d}t}\langle \mathrm{G}_i\rangle - \tfrac{\mathrm{d}}{\mathrm{d}t}\langle \mathrm{B}_i\rangle = \mu\langle \mathrm{B}_i\rangle - \lambda\langle \mathrm{A}_i\rangle,
\end{aligned}
\quad \xRightarrow[\frac{1}{N}\sum_i^N]{} \quad
\begin{aligned}
\frac{\mathrm{d}}{\mathrm{d}t}\langle [\mathrm{G}]\rangle &= \lambda\langle [\mathrm{A}]\rangle - \phi\langle [\mathrm{G}]\rangle - \rho_\mathrm{g}\langle [\mathrm{GB}]\rangle, \\
\frac{\mathrm{d}}{\mathrm{d}t}\langle [\mathrm{B}]\rangle &= \phi\langle [\mathrm{G}]\rangle - \mu\langle [\mathrm{B}]\rangle + \rho_\mathrm{g}\langle [\mathrm{GB}]\rangle, \\
\frac{\mathrm{d}}{\mathrm{d}t}\langle [\mathrm{A}]\rangle &= \mu\langle [\mathrm{B}]\rangle - \lambda\langle [\mathrm{A}]\rangle,
\end{aligned}
\tag{S1}$$

where $\langle\cdot\rangle$ are ensemble averages, $[\mathrm{x}]$ the domain fraction of species x, and $[\mathrm{xy}]$ the total number of neighbouring xy pairs divided by N, later referred to as the xy interface or xy perimeter. This set of equations can be derived rigorously from the master equation [e.g. 54]. To go from individual (left) to population level (right), we summed over i and divided by N, using Eq. M1. Section S2A is not a closed system. To close the system, we need to determine all undetermined terms $[\mathrm{xy}]$ on the right-hand side without creating new unknowns. The simplest way to do this is to assume absence of pairwise correlations, i.e. $\langle[\mathrm{xy}]\rangle = 4\langle[\mathrm{x}]\rangle\langle[\mathrm{y}]\rangle$. We take the additional assumption of $N \to \infty$, such that the law of large numbers applies and $[\mathrm{x}] \to \langle[\mathrm{x}]\rangle$. These assumptions are valid when all cells in an large domain interact with each other at uniform contact rates of order $1/N$. This results in the *simple mean-field approximation* of the GBA process:

$$\begin{aligned}
[\dot{\mathrm{G}}] &= \lambda[\mathrm{A}] - \phi[\mathrm{G}] - 4\rho_\mathrm{g}[\mathrm{G}][\mathrm{B}], \\
[\dot{\mathrm{B}}] &= \phi[\mathrm{G}] - \mu[\mathrm{B}] + 4\rho_\mathrm{g}[\mathrm{G}][\mathrm{B}], \\
[\dot{\mathrm{A}}] &= \mu[\mathrm{B}] - \lambda[\mathrm{A}],
\end{aligned}
\tag{S2}$$

where we also used the dot notation for time derivatives. Substituting $[\mathrm{A}] = 1 - [\mathrm{G}] - [\mathrm{B}]$ and taking only the

independent equations, we finally obtain

$$[\dot{\mathrm{G}}] = \lambda(1 - [\mathrm{G}] - [\mathrm{B}]) - \phi[\mathrm{G}] - 4\rho_{\mathrm{g}}[\mathrm{G}][\mathrm{B}], \tag{S3}$$
$$[\dot{\mathrm{B}}] = \phi[\mathrm{G}] - \mu[\mathrm{B}] + 4\rho_{\mathrm{g}}[\mathrm{G}][\mathrm{B}].$$

We further focus on the case $\phi = 0$, the reason for which will become clear below. When $\phi = 0$, Eq. S3 has two steady states, a trivial one at $([\mathrm{G}], [\mathrm{B}]) = (1, 0)$ and one at $([\mathrm{G}], [\mathrm{B}]) = (\frac{\mu}{4\rho_{\mathrm{g}}}, \frac{1-\mu/4\rho_g}{1+\mu/\lambda})$. The eigenvalues of the Jacobian of Eq. S3 show that for $4\rho_{\mathrm{g}}/\mu > 1$, the trivial steady states is a saddle and the non-trivial a spiral sink. For $4\rho_{\mathrm{g}}/\mu < 1$, the trivial state state is a stable node and the only physical solution. Hence, the steady states exchange stability at the transcritical bifurcation at $4\rho_{\mathrm{g}}/\mu = 1$. The GBA process with $\phi = 0$ is equivalent to the SIRS spreading process in epidemiology [42], which represents spread of a disease in a population with waning immunity. Fire B plays the role of infected individuals. Infections spread through a population of susceptibles G at rate ρ_{g} per GB link. They subsequently acquire a state of immunity A at rate μ, which can be lost at rate λ. The non-trivial steady state corresponds to the endemic equilibrium and the transcritical bifurcation to the epidemic threshold R_0.

B. Extinction in finite systems

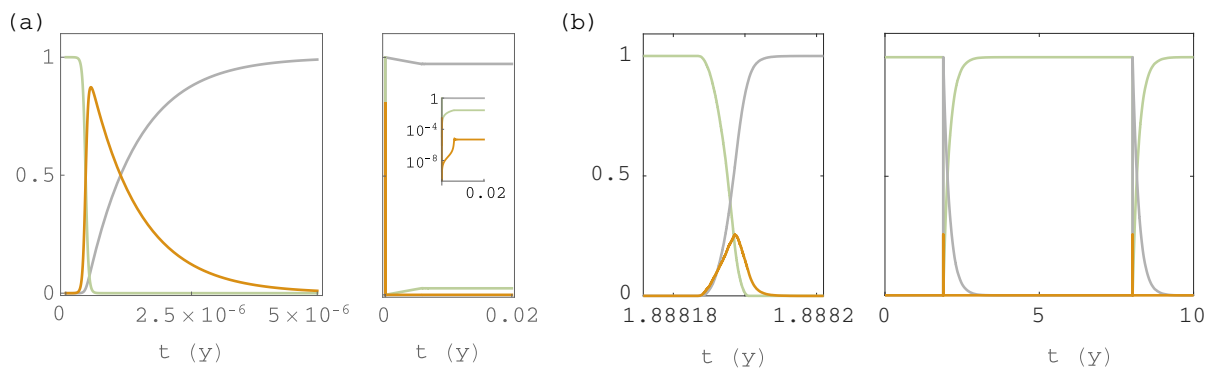

FIG. S5. Time series of the GBA process ($\lambda, \phi \neq 0$): (a) mean-field approximation, (b) simulation on a square lattice. G: green, B: orange, A: grey.

A well-known characteristic of this spreading process with $\phi = 0$ and $[\mathrm{B}]_0 > 0$ is that in finite systems, it goes extinct in finite time, even when $R_0 > 1$ [55]. This is so because stochastic excursions away from the non-trivial equilibrium will eventually reach the absorbing trivial state. When the spontaneous ignition rate $\phi > 0$ and the time to extinction is much smaller than the typical waiting time between ignition events, there are repeated fire events separated by extinction events. The dynamics then effectively behave as a series of GBA processes with $\phi = 0$ and $[\mathrm{B}]_0 > 0$. This is what we observe in cellular automaton simulations on a square lattice of 100×100 cells for realistic parameters (Fig. S5b, right panel). The mean-field approximation (Eq. S3), on the other hand, does not show extinction due to its assumption of $N \to \infty$. Instead, it shows a single pulse (Fig. S5a, left panel) after which a high-ash low-grass and non-zero fire steady state (the endemic equilibrium) is reached (Fig. S5a, right panel). In the case $\phi = 0$, the required lattice size to avoid extinction with high probability depends on the initial conditions [55], but for realistic parameter ranges, it is unrealistically large. This can be understood as follows.

- When the initial condition is a single fire, at least one cell has to keep on burning until the density of grass has regrown to a level sufficient for a new wave to propagate. This translates into the condition $(L/\Delta x)^2 \exp(-\mu/\lambda) \geq \mathcal{O}(1)$, such that $L \geq \mathcal{O}(10^{4 \cdot 10^4})$ for our parameters (taking a grid size of $\Delta x = 0.03$km as in [12]).
- When initial conditions are such that a band of the domain is immune at the start, a single fire can keep on burning by crossing the domain repeatedly [55]. When assuming $\rho_{\mathrm{g}} \gg \mu$ and using that waiting times between spreading events are exponentially distributed with mean $1/\rho_{\mathrm{g}}$, a fire will spread throughout the domain in a time of the order $\tau \approx L/(\rho_{\mathrm{g}}\Delta x)$. For there to be sufficient regrowth of grass on this time scale, we need $L/(\rho_{\mathrm{g}}\Delta x) \approx 1/\lambda$, or $L \approx \rho_{\mathrm{g}}\Delta x/\lambda$. For the parameters we have chosen, this means $L = \mathcal{O}(10^4)$km, i.e. the order of magnitude of the earth's circumference, which is drastically smaller than the above estimate yet still impractically large.

Taking more conservative estimates for fire spreading rates or taking account of a small positive fire ignition rate $\phi = \mathcal{O}(\lambda/N)$ for the initial condition with a single burning cell, this may be decreased by an order of magnitude, i.e. the size of a continent. Still, in reality, extinction will occur on smaller scales due to spatiotemporal heterogeneity of forcing parameters as a consequence of climatic seasonality or existence of natural or artificial boundaries (such as forests), leading to a lower effective system size. Hence, in any real system, repeated extinction and system-scale oscillations are to be expected.

C. Percolation analysis of a single fire event

Therefore, a single fire in realistically sized systems corresponds to the case $\phi = 0$, starting with a single burning cell. Using that the regrowth of grass occurs on a much slower time scale, we can further also set $\lambda = 0$ in our following analysis. The GBA process with $\phi, \lambda = 0$ is equivalent to susceptible-infected-recovered (SIR) epidemic spreading [42]. The final size of the epidemic in SIR epidemic spreading on a lattice shows a continuous phase transition (CPT) at a critical spreading rate ρ_{g} and scaling laws near the critical point obey those of the ordinary percolation universality class [56]. Figure S6 shows mean quantities for SIR epidemic spreading on a square lattice in a range of infection probabilities and initial number of immune individuals, which are spatially uniformly distributed. In particular, we show that SIR epidemic spreading is a type of *mixed site-bond percolation*, with bond occupation probability given by $p_b := p_{\mathrm{g}} = \rho_{\mathrm{g}}/(\rho_{\mathrm{g}} + \mu)$ (which is fixed at 0.9 in the main text, as in ref. [12]) and site occupation probability given by $p_s := [\mathrm{G}]_0$, i.e. the initial fraction of cells that are grass in fire spreading, or the complement of the initial fraction of immune individuals in epidemic spreading (with the rest being susceptible). In Fig. S6, we record the *mean cumulative burning probability of being burnt* $\langle Q \rangle$ and the *susceptibility* χ of $\langle Q \rangle$, defined as

$$Q := \frac{[\mathrm{A}]^* - [\mathrm{A}]_0}{[\mathrm{G}]_0}, \tag{S4}$$

$$\chi = \frac{\langle Q^2 \rangle}{\langle Q \rangle}, \tag{S5}$$

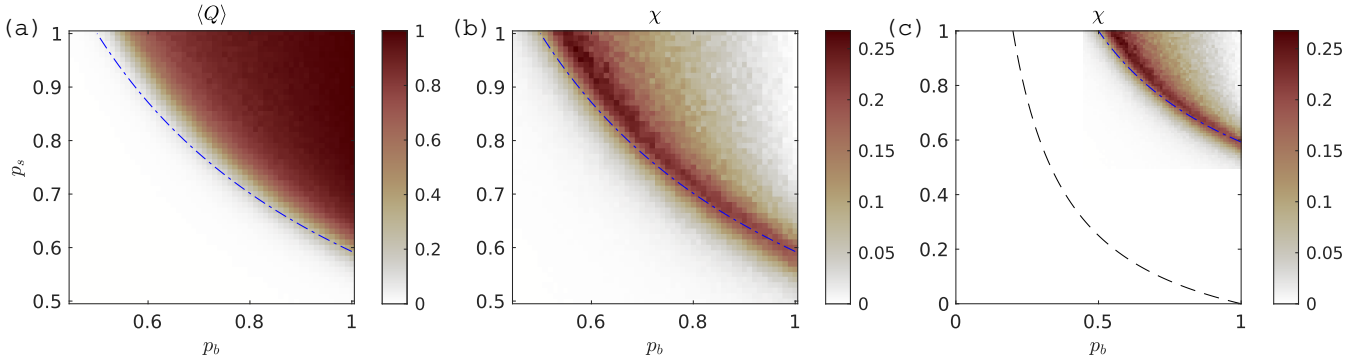

FIG. S6. GBA process with ϕ=λ=0 (equivalent to square lattice SIR spreading): $\langle Q \rangle, \chi$ versus bond occupation probability $p_b := p_{\mathrm{g}}$ (Eq. 3) and site occupation probability p_s=$[\mathrm{G}]_0$. (a) Mean cumulative probability of being burnt $\langle Q \rangle$ (expectation of Eq. S4). (b) Susceptibility χ (Eq. S5). (c) Susceptibility χ compared to the mean-field percolation threshold $p_{s,\mathrm{mf}}$, given in Eq. S6 (dashed black). The dash-dotted blue line indicates the location of the infinite-size percolation threshold for uncorrelated mixed site-bond percolation (taken from [53]). The GBA model's percolation threshold lies at higher values (b) due to spatial correlation of p_{g} as explained in the text. The colour scale was taken from [57]. See Fig. S12 for more detail.

where $[\cdot]_0$ denotes initial value and $[\cdot]^*$ final value. For $N \to \infty$, $\langle Q \rangle$ converges to the *percolation probability* P_∞, which is the probability that a grass cell belongs to the giant connected component. We use the location where χ peaks as an estimate of the percolation threshold [17, 58]. When $p_s = [\mathrm{G}]_0 = 1$, we have pure bond percolation and when $\rho_{\mathrm{g}}/\mu \to \infty$, we have pure site percolation. The percolation threshold for standard mixed site-bond percolation (from [53]) is shown in Fig. S6 with a dot-dashed blue curve. The pure bond percolation threshold (when $[\mathrm{G}]_0 = 1$) of SIR epidemic spreading occurs at higher p_b than in standard bond percolation ($p_b \approx 0.538 > 0.5$) because the possibility of spreading to multiple neighbours makes the bond occupation probability spatially autocorrelated, as shown by [56]. The pure site percolation limit shows the classical value (for the square lattice) of $[\mathrm{G}]_0 \approx 0.593$. From Eq. S3 (with $\phi = \lambda = 0$), we can obtain the mean-field percolation threshold $p_{s,\mathrm{mf}}$ by finding where the trivial state becomes unstable in Eq. S3, which is given by

$$4[\mathrm{G}]_0 \frac{\rho_{\mathrm{g}}}{\mu} = 1 \implies p_{s,\mathrm{mf}} = [\mathrm{G}]_0 = \frac{1}{4}\left(\frac{1}{p_b} - 1\right). \tag{S6}$$

As shown in Fig. S6c, the mean-field approximation shows a large bias towards lower values.

Implications for the FGBA process On landscapes with forest, fires can be blocked (albeit imperfectly) by forest cells. These landscapes obtain a steady state shape due to the shaping processes of forest demography and fire. Hence, results from the spatially uniform $[\mathrm{G}]_0$ above do not apply to percolation effects in the full FGBA process. That is, when fire spreads on landscapes with forest, the critical point for pure site percolation ($\rho_\mathrm{g}/\mu \to \infty$, or $p_\mathrm{g} \to 1$) will in general depend not only on the site occupation probability $[\mathrm{G}]_0$ but also on the spatial correlation function of site occupation. For the idealised case of fire-proof forest ($p_\mathrm{f} = 0$), fire percolation on real landscapes is then equivalent to *correlated mixed percolation*, where correlations in bond occupation probability occur due to the spreading process, and correlations in site occupation probability occur due to the nonrandom spatial structure of the landscape. When $p_\mathrm{f} > 0$, the spreading process becomes a *heterogeneous (correlated) bond percolation processes*, i.e. a percolation process in which fire spread on grass occurs with bond occupation probability p_g and on forest with bond occupation probability p_f. The possibility of spreading on forest decreases the percolation thresholds compared to the correlated mixed percolation limit of $p_\mathrm{f} \to 0$. This decrease is expected to be small because forests do not spread fires well ($p_\mathrm{f} \approx 0$).

S3. SIMPLE MEAN FIELD OF JOINT FOREST AND FIRE SPREAD

When we follow the same steps as in S2A, we obtain the *simple mean-field approximation* of the FGBA process:

$$\begin{aligned}
[\dot{\mathrm{G}}] &= \lambda[\mathrm{A}] - \phi[\mathrm{G}] - 4\rho_\mathrm{g}[\mathrm{G}][\mathrm{B}] - \beta[\mathrm{G}] - 4\alpha[\mathrm{F}][\mathrm{G}] + \gamma[\mathrm{F}],\\
[\dot{\mathrm{F}}] &= \beta[\mathrm{A}] + 4\alpha[\mathrm{F}][\mathrm{A}] - 4\rho_\mathrm{f}[\mathrm{F}][\mathrm{B}] + \beta[\mathrm{G}] + 4\alpha[\mathrm{F}][\mathrm{G}] - \gamma[\mathrm{F}],\\
[\dot{\mathrm{B}}] &= \phi[\mathrm{G}] - \mu[\mathrm{B}] + 4\rho_\mathrm{f}[\mathrm{F}][\mathrm{B}] + 4\rho_\mathrm{g}[\mathrm{G}][\mathrm{B}],\\
[\dot{\mathrm{A}}] &= \mu[\mathrm{B}] - \lambda[\mathrm{A}] - \beta[\mathrm{A}] - 4\alpha[\mathrm{F}][\mathrm{A}].
\end{aligned} \tag{S7}$$

The simple mean field shows bistability of tree cover (first shown by ref. [12] for $\gamma = 0$) in ranges of all parameters that are expected to show considerable spatial heterogeneity in a given ecosystem: $\alpha, \beta, \gamma, \phi$ (Fig. S7). However, despite being qualitatively correct, it shows a large bias compared to simulations. For the parameter ranges of our simulations, it has no non-trivial solution for positive fire ignition rate ϕ, so we had to choose different parameter values to find its bistability range. This bias is due to the inability of the simple mean to capture two effects: repeated fire extinction on a fast timescale and the spatial nature of the two spreading processes. In the following section, we derive alternative mean-field models that partially correct for these biases.

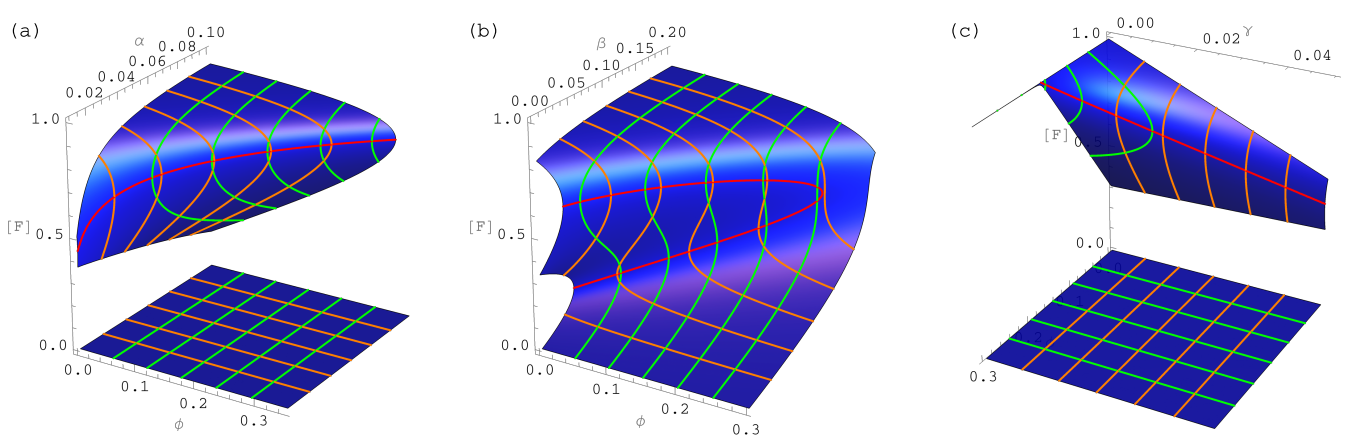

FIG. S7. Steady states and bifurcations of forest cover [F] in the simple mean field of the FGBA process (blue: steady state manifold, green/orange contours at fixed axis values, red: saddle-node bifurcations): (a) versus fire ignition rate ϕ and forest spreading rate α, (b) versus fire ignition rate ϕ and spontaneous forest growth rate β, (c) versus fire ignition rate ϕ and spontaneous forest mortality rate γ. Due to its large bias, the simple mean field shows different bistability ranges than the simulations. We set p_g=0.25 (requiring a ρ_g that is 27x smaller than in simulations) such that bistability ranges are visible (remaining parameters are as in Table M1).

S4. TWO-TIMESCALE MEAN FIELD OF JOINT FOREST AND FIRE SPREAD

Here, we derive an alternative mean-field model that takes account of separation of fire events in systems with realistic sizes, assuming that fire spread occurs on a much faster time scale than forest spread. This means that we can consider the fire spreading process in isolation with $\phi = \lambda = 0$ (as argued in Section S2), and take the asymptotic amount of forest burnt by a single fire before extinction on the fast time scale as forest mortality per fire event on the slow time scale.

A. Well-mixed fire and forest

We start with the simplest case, where both vegetation and fire mix uniformly.

1. *Fast process: forest loss due to a single fire*

On the fast time scale, we can set all small parameters related to forest demography, grass regrowth and fire ignition to zero (α=β=γ=λ=ϕ=0), such that we obtain

$$\begin{aligned}
\frac{\mathrm{d}}{\mathrm{d}t}[\mathrm{G}] &= -4\rho_\mathrm{g}[\mathrm{G}][\mathrm{B}],\\
\frac{\mathrm{d}}{\mathrm{d}t}[\mathrm{F}] &= -4\rho_\mathrm{f}[\mathrm{F}][\mathrm{B}],\\
\frac{\mathrm{d}}{\mathrm{d}t}[\mathrm{B}] &= -\mu[\mathrm{B}] + 4\rho_\mathrm{f}[\mathrm{F}][\mathrm{B}] + 4\rho_\mathrm{g}[\mathrm{G}][\mathrm{B}],\\
\frac{\mathrm{d}}{\mathrm{d}t}[\mathrm{A}] &= \mu[\mathrm{B}],
\end{aligned} \tag{S8}$$

where the products arise from the well-mixedness assumption as before. By rewriting the equations for $\frac{\mathrm{d}}{\mathrm{d}t}[\mathrm{G}]$, $\frac{\mathrm{d}}{\mathrm{d}t}[\mathrm{F}]$, $\frac{\mathrm{d}}{\mathrm{d}t}[\mathrm{A}]$ as

$$-\frac{1}{4\rho_\mathrm{g}[\mathrm{G}]}\frac{\mathrm{d}}{\mathrm{d}t}[\mathrm{G}] = -\frac{1}{4\rho_\mathrm{f}[\mathrm{F}]}\frac{\mathrm{d}}{\mathrm{d}t}[\mathrm{F}] = \frac{1}{\mu}\frac{\mathrm{d}}{\mathrm{d}t}[\mathrm{A}] = [\mathrm{B}], \tag{S9}$$

we can obtain [G] and [F] as a function of [A] via separation of variables and integration:

$$[\mathrm{G}](t) = [\mathrm{G}]_0 \exp\big(-\frac{4\rho_\mathrm{g}}{\mu}[\mathrm{A}](t)\big), \quad [\mathrm{F}](t) = [\mathrm{F}]_0 \exp\big(-\frac{4\rho_\mathrm{f}}{\mu}[\mathrm{A}](t)\big). \tag{S10}$$

Substituting Eq. S10 into the equation for $\frac{\mathrm{d}}{\mathrm{d}t}[\mathrm{A}]$ in Eq. S8 and setting the time derivative to zero, we obtain an implicit relation of the asymptotic amount of vegetation burnt:

$$[\mathrm{A}]^* = 1 - [\mathrm{G}]^* - [\mathrm{F}]^* = 1 - [\mathrm{G}]_0 \exp\big(-\frac{4\rho_\mathrm{g}}{\mu}[\mathrm{A}]^*\big) - [\mathrm{F}]_0 \exp\big(-\frac{4\rho_\mathrm{f}}{\mu}[\mathrm{A}]^*\big). \tag{S11}$$

When taking an initial state consisting of only grass and forest, that is $[\mathrm{G}]_0 = 1 - [\mathrm{F}]_0$, $[\mathrm{A}]^*$ can be found numerically as a function of ρ_g/μ, ρ_f/μ and $[\mathrm{F}]_0$. This can in turn be used to obtain the total amount of forest lost due to a single fire, from Eq. S10,

$$\Delta[\mathrm{F}]_\mathrm{mf} := [\mathrm{F}]_0 - [\mathrm{F}]^* = [\mathrm{F}]_0\Big(1 - \exp\big(-\frac{4\rho_\mathrm{g}}{\mu}[\mathrm{A}]^*\big)\Big), \tag{S12}$$

where subscript mf denotes mean field. A plot of Equation S12 versus [F] is given in Fig. S8 (solid purple curve), which shows that the percolation threshold – where forest starts blocking fire – lies at unrealistically low grass cover, as was also the case for perfectly blocking forest (Fig. S6c, dashed line).

2. *Slow processes: forest demography and fire damage*

Now, we can define the mean-field forest gain and loss terms on the slow time scale as

$$\Delta^{\text{gain}}_{\text{F,mf}} := \beta[\text{G}] + 4\alpha[\text{F}][\text{G}] - \gamma[\text{F}], \tag{S13}$$

$$\Delta^{\text{loss}}_{\text{F,mf}} := \phi N[\text{G}]\Delta[\text{F}]_{\text{mf}}, \tag{S14}$$

such that the final mean-field model becomes

$$\begin{aligned}\frac{\text{d}}{\text{d}t}[\text{F}] &= \Delta^{\text{gain}}_{\text{F,mf}} - \Delta^{\text{loss}}_{\text{F,mf}} \\ &= \beta[\text{G}] + 4\alpha[\text{F}][\text{G}] - \gamma[\text{F}] - \phi N[\text{G}]\Delta[\text{F}]_{\text{mf}}, \\ &= \beta(1-[\text{F}]) + 4\alpha[\text{F}](1-[\text{F}]) - \gamma[\text{F}] - \phi N(1-[\text{F}])[\text{F}]\Big(1 - \exp\big(-\frac{4\rho_{\text{g}}}{\mu}[\text{A}]^*([\text{F}])\big)\Big).\end{aligned} \tag{S15}$$

The steady states are shown in Fig. S10 in solid purple for the same parameters as those used in the simulations of the main text. For low and high tree cover, it reproduces the steady states fairly accurately, but unlike the simulations, it shows no wide saddle in between. Hence, while this is an improvement compared to the simple mean field, there is still a large bias at intermediate tree cover. To address this bias, we need drop the assumption of uniform mixing for fire spread.

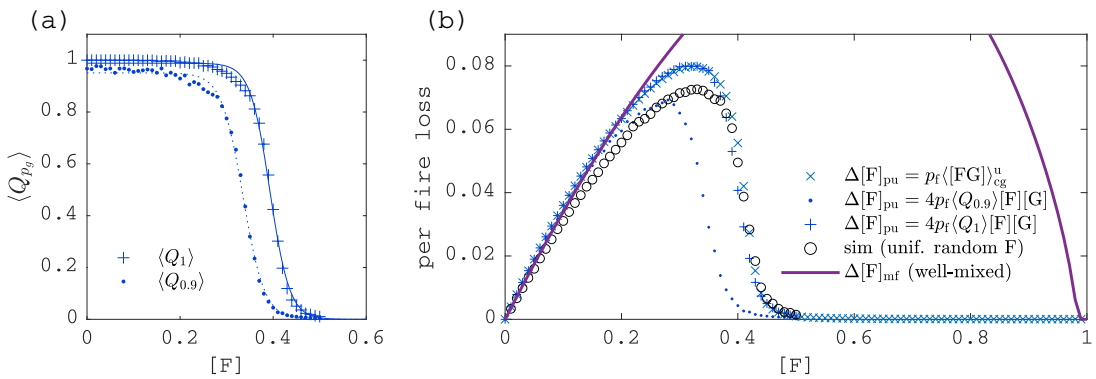

FIG. S8. Grass burning probabilities and forest loss per fire in uniformly random landscapes: (a) probability that a grass cell burns $\langle Q_{p_{\text{g}}}\rangle$, for $p_{\text{g}} = 1$ ('+') and for $p_{\text{g}} = 0.9$ ('·'), together with fits to logistic functions; (b) loss per fire estimated from grassland-weighted forest ('×', Eq. S16), from $\langle Q_{0.9}\rangle$ ('×', Eq. S20), from $\langle Q_1\rangle$ ('+', Eq. S20), by assuming uniform mixing (purple curve, Eq. S12), and measured in fire simulations with uniform random placement of forest ('○').

B. Spatial fire percolation and uniformly random forest

While the uniform mixing assumption may be ecologically justified for forest spread in case of species with long-range seed dispersal, it is much harder to justify for fire spread, which is fundamentally a local contagion process. Therefore, we aim to take into account the effects of fire as a percolation process while still assuming absence of spatial correlations between forest cells. Because the percolation process affects forest loss, this only affects the loss function. Earlier mean-field models [9–11] accounted for the effects of fire percolation on tree mortality by making fire-affected rates sigmoid functions of tree cover, such as those shown in Fig. S8a, while assuming that vegetation remains well-mixed throughout the domain or in a subregion (see [10] for the best justified account in case of savannas). Therefore the mean-field analyses presented here provide the fairest points of comparison.

To estimate the loss due to fire, we will show two alternative approaches. The first is equivalent to our approach in the main text, using grassland-weighted forest perimeter to estimate exposed forest. The second estimates exposed forest via standard results from percolation theory, which are valid here due to the assumption of uniform random placement of forest.

1. Using the *grassland-weighted forest perimeter* $\langle[\text{FG}]\rangle_{\text{cg}}$ (see Eq. 7). According to this approach, fires spread perfectly to the forest perimeter, where a fraction of the forest is burnt. The difference with the main text is

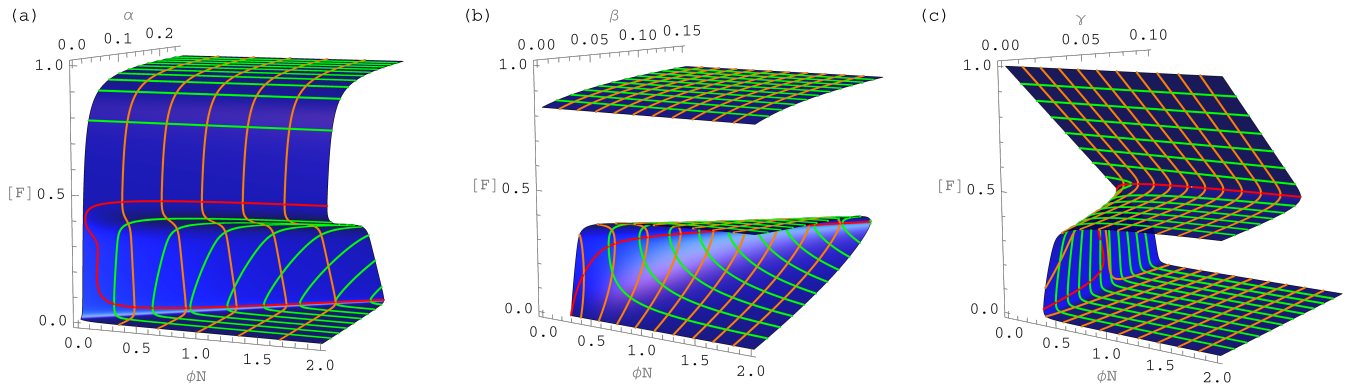

FIG. S9. Steady states and bifurcations of forest cover [F] in the two-timescale mean field of the FGBA process via Eq. S18 (blue: steady state manifold, green/orange contours at fixed axis values, red: saddle-node bifurcations) as a function of (scaled) fire ignition rate ϕN and: (a) forest spreading rate α, (b) spontaneous forest growth rate β, (c) spontaneous forest mortality rate γ. Parameters others than the ones on the axes are the same as those chosen in simulations – see Table M1.

that the landscapes in which fire spreads have uniform random placement of forest. We indicate this difference below by the superscript u in $\langle[\mathrm{FG}]\rangle^{\mathrm{u}}_{\mathrm{cg}}$. The resulting loss per fire is

$$\Delta[\mathrm{F}]_{\mathrm{pu}} = p_{\mathrm{f}}\langle[\mathrm{FG}]\rangle^{\mathrm{u}}_{\mathrm{cg}}, \tag{S16}$$

such that the loss function is

$$\Delta^{\mathrm{loss}}_{\mathrm{F,pu}} = \phi N[\mathrm{G}]\Delta[\mathrm{F}]_{\mathrm{pu}} = \phi N p_{\mathrm{f}}[\mathrm{G}]\langle[\mathrm{FG}]\rangle^{\mathrm{u}}_{\mathrm{cg}}, \tag{S17}$$

where subscript pu refers to percolation on a square lattice with uniform random placement of forest. The final mean-field model is

$$\begin{aligned}\frac{\mathrm{d}}{\mathrm{d}t}[\mathrm{F}] &= \Delta^{\mathrm{gain}}_{\mathrm{F,mf}} - \Delta^{\mathrm{loss}}_{\mathrm{F,pu}},\\ &= \beta(1-[\mathrm{F}]) + 4\alpha[\mathrm{F}](1-[\mathrm{F}]) - \gamma[\mathrm{F}] - \phi N p_{\mathrm{f}}(1-[\mathrm{F}])\langle[\mathrm{FG}]\rangle^{\mathrm{u}}_{\mathrm{cg}}([\mathrm{F}]),\end{aligned} \tag{S18}$$

where we made explicit that $\langle[\mathrm{FG}]\rangle^{\mathrm{u}}_{\mathrm{cg}}$ is a function of [F]. This mean-field model shows clear bistability for the same parameter ranges as in simulations (Fig. S9). For the exact same parameters, this mean-field is qualitatively most comparable to simulations, but the saddle is much flatter (Fig. S10, solid blue line versus black dots).

2. Using *percolation theory*. Alternatively, we can estimate forest loss using mean burning probabilities from percolation due to a single fire. The forest perimeter exposed to fire for a given realisation is the interface of burnt grass with forest at the end of the fire $[\mathrm{FA}]^*$. When we take the expectation (for given total grass cover) and forest cells are assumed to be uniformly randomly placed, we have

$$\langle[\mathrm{FA}]^*\rangle = \langle 4[\mathrm{F}][\mathrm{A}]^*\rangle = 4[\mathrm{F}][\mathrm{G}]\langle Q_{p_{\mathrm{g}}}\rangle, \tag{S19}$$

where $\langle Q_{p_{\mathrm{g}}}\rangle$ is the mean proportion of grass that burns for given p_{g} and [G] (see Eq. S4; shown in Fig. S6b). The loss per fire in this case is then

$$\Delta[\mathrm{F}]_{\mathrm{pu}} = 4p_{\mathrm{f}}[\mathrm{F}][\mathrm{G}]\langle Q_{p_{\mathrm{g}}}\rangle, \tag{S20}$$

such that the loss function is (multiplying by $\phi N[\mathrm{G}]$)

$$\Delta^{\mathrm{loss}}_{\mathrm{F,pu}} = 4p_{\mathrm{f}}\phi N[\mathrm{G}]^2[\mathrm{F}]\langle Q_{p_{\mathrm{g}}}\rangle. \tag{S21}$$

The final mean-field model is then

$$\frac{\mathrm{d}}{\mathrm{d}t}[\mathrm{F}] = \beta(1-[\mathrm{F}]) + 4\alpha[\mathrm{F}](1-[\mathrm{F}]) - \gamma[\mathrm{F}] - 4p_{\mathrm{f}}\phi N(1-[\mathrm{F}])^2[\mathrm{F}]\langle Q_{p_{\mathrm{g}}}\rangle. \tag{S22}$$

This mean-field model has very similar steady states as Eq. S18 but the saddle is slightly lower (dotted blue line in Fig. S10). In the limit of large domain size, $\langle Q_{p_{\mathrm{g}}}\rangle$ may be replaced by the percolation probability P_∞, which is defined as the probability that a grass cell belongs to the giant component [18] (see also Fig. S12a).

Both of the estimates above assume that $p_\mathrm{f} = 0$ for fire spread and that p_f is small for loss of (uniformly randomly placed) forest due to fire. The first further assumes that fire spreads perfectly on grass ($p_\mathrm{g} = 1$). Therefore the two estimates are equivalent when the spreading process is pure site percolation, for which $\langle[\mathrm{FG}]\rangle_\mathrm{cg} = 4\langle Q_1\rangle[\mathrm{F}][\mathrm{G}]$ (equating Eq. S17 and Eq. S21), which is confirmed by Fig. S8b ('×' and '+' symbols). Comparing the estimates to recorded forest loss in fire simulations where only the assumption of random placement is taken ('∘' in Fig. S8b), one sees that the second estimate ('·' in Fig. S8b) is more accurate than the first estimate ('×' in Fig. S8b), despite that it carries more assumptions. Hence, the error due to the assumption of grass perfectly spreading compensates the error by the assumption of forest perfectly blocking fire. We expect that the difference between the two approaches will be smaller for landscapes with spatial aggregation of forest, where fires spread in pockets of high grass cover, for which $\langle Q_1\rangle - \langle Q_{0.9}\rangle$ is smaller (Fig. S8a).

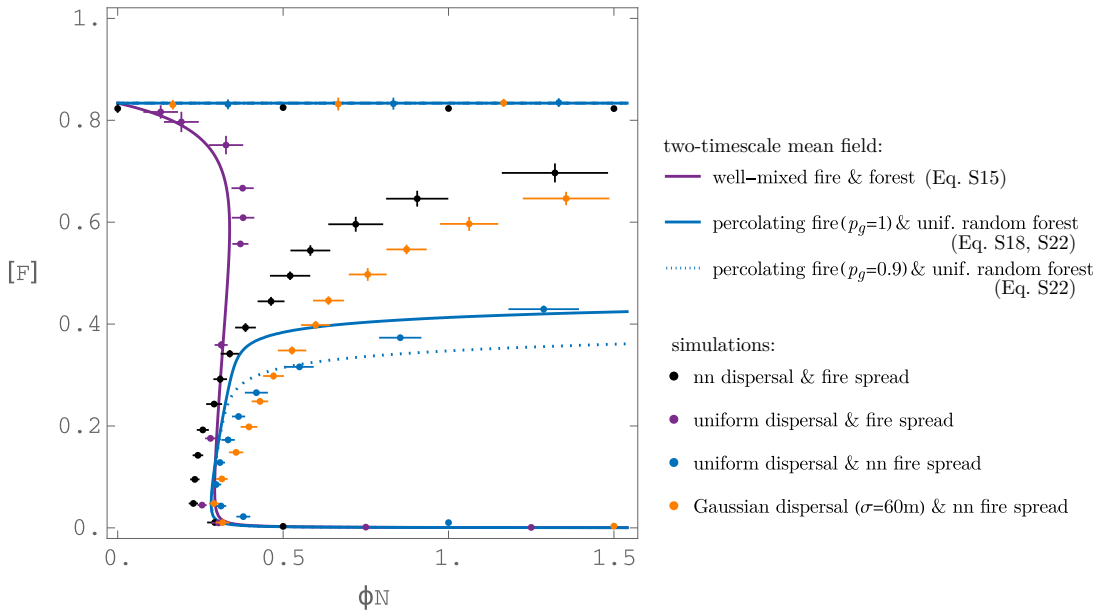

FIG. S10. Comparison of steady state forest as a function of ignition rate in the time-separated mean-field and in simulations (dots with error bars: simulations, lines: mean field). See legend for details.

C. Detailed comparison against simulations

Here, we compare the time-separated mean-field models to the simulations of the main text and also to other simulations with different spreading ranges for forest and/or fire. In Fig. S10, dots with error bars are simulations and lines are mean-field approximations. The black dots are the simulations from the main text, with nearest-neighbour spreading for both fire and forest. Purple dots are simulations where both fire and forest can spread to any other cell. Blue dots are simulations where forest can spread to any other cell, but fire spreads along nearest neighbours. And finally, orange dots denote simulations where forest spread occurs in a Gaussian neighbourhood with standard deviation 60m (two cells).

All simulations and approximations agree fairly well on the parameter value where the lower saddle-node bifurcation occurs. All except the fully well-mixed case agree on the stable steady states. The disagreement occurs particularly for the unstable steady states, where the effect of spatial structure is hence most pronounced and process-dependent. There is little or no bistability in the well-mixed two-timescale mean-field (purple line) but its good agreement with uniformly mixed simulations (purple dots) further indicates the validity of the assumption of time-scale separation with well-separated fire events. The mean field where fire is a site percolation process on landscapes with uniform random placement of forest (blue line), is qualitatively more correct but it has a much flatter saddle than the simulations (black dots). Hence, even the mean-field model that takes into account the effects of percolation while keeping forest cells spatially uncorrelated remains strongly biased due to the importance of spatial aggregation of forest cells. Taking larger neighbourhood sizes in the simulations does not change this (orange dots). Even compared to simulations with uniform forest dispersal (blue dots), the mean field with site percolation shows some bias, indicating that the fire spreading alone already induces some spatial structure. This is most likely caused by lower survival rates of solitary compared to aggregated forest cells.

The bias of the mean field is even more apparent in the dynamics. Figure S3 shows the same figure as Fig. 4, but with the corresponding values of the mean field with site percolation on top. Panels a–c show large differences

between [FG] and $\langle[\mathrm{FG}]\rangle_{\mathrm{cg}}$ of simulations (scattered dots) versus those from the mean field (curves). In particular, while for the mean field, the perimeter is the parabola $[\mathrm{FG}] = 4[\mathrm{F}][\mathrm{G}] = 4[\mathrm{F}](1-[\mathrm{F}])$, the perimeter of simulations lies below this parabola for any [F]. That the simulated perimeter is lower for given forest area means that forest is more spatially aggregated in simulations. This results in lower forest growth rate at any cover value (panels d–f) because fewer forest cells can expand into grass. Fire-induced damage is lower below $[\mathrm{F}] \approx 0.4$ and higher above (panels d–f). This is so because damage per fire (at given cover) is determined by two effects: exposure of forest and clustering of grass. Below $[\mathrm{F}] \approx 0.4$, there is no clustering, such that only decreased exposure due to aggregation can decrease forest loss. Above $[\mathrm{F}] \approx 0.4$, aggregation decreases clustering, such that grassland stays fully connected at higher forest cover than in the uniformly random case, with larger fires as a consequence. This further leads to an upward shift of the unstable forest state compared to the mean field (panels (g–i), see also Fig. S10). The effect of forest aggregation on the fire dynamics on the fast time scale is well-known from the equivalent effect in disease spread: in the SIR process, aggregation of immunise individuals lowers the epidemic threshold, such that it elevates the population immunisation threshold to eradicate the epidemic [23]. Note though, that, as argued above, the equivalent epidemic process to tropical fire spread in forest-grassland landscapes is not the regular SIR process, but one that has a mix of two populations: susceptibles (grass) and imperfectly immunised individuals (forest).

S5. EVOLUTION OF FRONTS — HETEROGENEOUS STATES

Here, we illustrate the case where grass and forest are initially separated into two contiguous areas with their interface extending along a straight line. Because for this type of initial conditions, the single-cluster approximation (Eq. 11) is valid, we can focus on the evolution of the interface. As spontaneous conversion between forest and grass (with rates β and γ) increases mixing and promotes homogeneity at large scale, we expect the effects of heterogeneous initial conditions to be most persistent when the spontaneous conversion rates β and γ are small. Therefore, we will set $\beta = \gamma = 0$, for which Eq. 9 becomes

$$\frac{\mathrm{d}[\mathrm{F}]}{\mathrm{d}t} = (\alpha - \phi p_{\mathrm{f}} N[\mathrm{G}])[\mathrm{FG}]. \tag{S23}$$

Hence, the precise shape of the interface [FG] does not affect the location of the steady states, only the rate at which they are approached or receded from. The trivial steady states of Eq. S23 are $[\mathrm{F}] = 0$ and $[\mathrm{F}] = 1$ (where $[\mathrm{FG}] = 0$), which are stable, and between them, there is the saddle

$$[\mathrm{F}]^* = 1 - \frac{\alpha}{\phi N p_{\mathrm{f}}}. \tag{S24}$$

As seen in Fig. S13, this analytical prediction (solid black) matches the controlled simulations with $p_{\mathrm{g}} = 0.9999$ (shaded blue). For $p_{\mathrm{g}} = 0.9$ (shaded red), which we used before, there is a small bias. In the limit of $N \to \infty$, Eq. S24 converges to $[\mathrm{F}]^*_\infty = 1$, implying that in an infinite domain, any positive fire rate leads to extinction of forest below $[\mathrm{F}]^* = 1$. When ignoring the effect of ash, this would also occur for heterogeneous initial conditions. That is, considering an infinite domain with many grass clusters of which the size is a random variable (with support $[0, \infty)$), there will be initial grass clusters of arbitrarily large size, which will expand and eventually drive forest extinct. However, such determinism does not occur in the simulations because at high fire rates, patches with ash start to block fires, and the rate of exposure of the forest interface to fire becomes limited by the rate at which ash is converted back into grass. As a first correction for this, one can multiply p_{f} with the average proportion of grass sites that are in the ash state after the expected waiting time between fires $1 - \exp(-\lambda/\phi N)$, such that $[\mathrm{F}]^*_\infty = 1 - \alpha/\lambda p_{\mathrm{f}}$. Keeping in mind that we are focusing on heterogeneous states, the analysis here implies that for $\gamma = \beta = 0$, there is a critical patch size above which the forest patch expands and below which it contracts. The intuition is that above the critical forest patch size, there is not enough grass area to reach the minimum number of ignitions required to erode the forest.

In Fig. S11, we show how the dynamics and steady states arise from [FG], as we did in Fig. 3 and Fig. 4, but now starting with separated patches of grass and forest that interface on a line on both sides (showing for $[\mathrm{F}]_0 = 0.57$). From $[\mathrm{FG}](0) = 2L/N = 2N^{-1/2} = 0.02$, the interface quickly gains roughness due to the dynamics, until it reaches a steady state of $[\mathrm{FG}]^* \approx 6L/N = 6N^{-1/2} = 0.06$ (see Fig. S11a–c), which appears independent of ϕ (not shown). Figure S11b confirms that $\langle[\mathrm{FG}]\rangle_{\mathrm{cg}} \approx [\mathrm{FG}]$ (except when forest cover approaches $[\mathrm{F}] = 0$ or $[\mathrm{F}] = 1$), confirming that the single-cluster approximation is valid. Away from $[\mathrm{F}] = 0$ and $[\mathrm{F}] = 1$, [FG] stays about constant as the forest interface moves (Fig. S11b–c). Therefore the gain and loss terms (as defined in Eqs. 5 and 8) are now, respectively, constant and linearly decreasing with [F] (Fig. S11e), such that $\mathrm{d}[\mathrm{F}]/\mathrm{d}t$ increases linearly with [F] (Fig. S11g), except near $[\mathrm{F}] = 0$ and $[\mathrm{F}] = 1$, where it connects to 0, as here $[\mathrm{FG}] = 0$.

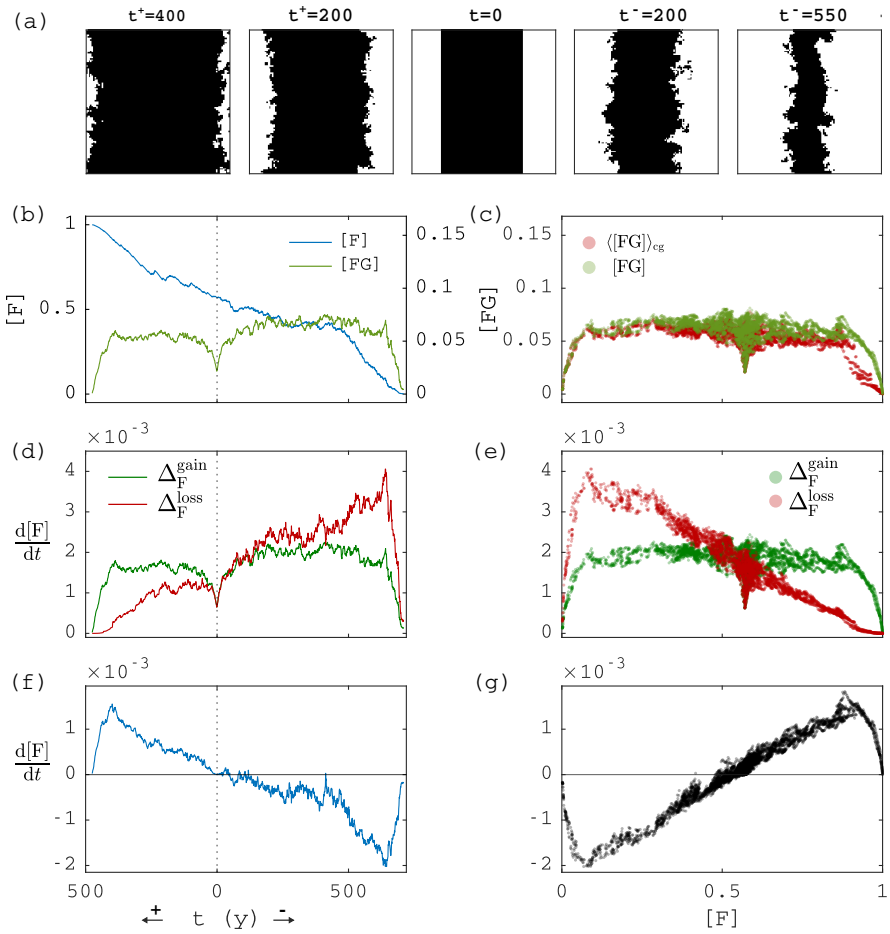

FIG. S11. Perimeter quantities and change rates according to Eq. 9 when initial conditions are heterogeneous and there are no spontaneous transitions (β=γ=0) for ϕ=6.98 · 10^{-5}, displayed as in Figs. 3 and 4. (a) Snapshots of the domain at indicated times. (b,d,f) Cover, interface and rate of change from Eq. 9 versus time. (c,e,g) Interface, grass-cluster weighted average of the interface, and rate of change from Eq. 9 versus cover. Remaining parameters are α=0.03, ρ_g=10^{10}, ρ_f=1.11 · 10^5, μ=10^6, λ=5.

S6. HOW TO INCLUDE FIRE PARAMETERS IN EXISTING MEAN-FIELD MODELS

Previously derived mean-field models of tropical tree cover bistability did not include parameters that relate to fire. Here we give suggestions on how to include fire ignition rate and the appropriate percolation quantities, focusing on the Staver-Levin mean-field model [9, 10] of tropical savanna and/or forest bistability. We assume the reader is familiar with [9, 10].

By running an infection process on clusters obtained by standard site percolation, [10] used a mixed site-uncorrelated bond-correlated percolation process for fire (although not using this terminology). The site percolation is due to uniformly randomly distributed tree cells perfectly blocking fires and the bond percolation due to flammable cells (grass and savanna saplings in [10]) spreading fires with a given probability. The correlation in bond occupation probability occurs due to the infection dynamics, as explained in Section S2C. One can use the complement of the burning probability of this mixed percolation process, i.e. $1 - \langle Q_{p_b}(p_s)\rangle$, as survival probability instead of that used in [10] (see Fig. S12b for a plot of $\langle Q_{p_b}(p_s)\rangle$ as a function of the infection probability between flammable cells p_b and the probability of a cell being flammable p_s). If one does so, one can write the mean-field recruitment rate of savanna saplings during a small time interval as $\omega(p_b, p_s)$[S], where ω is

$$\omega(p_b, p_s) := \max[\omega_0 - \phi N p_s \langle Q_{p_b}(p_s)\rangle \Delta\omega, 0], \tag{S25}$$

with $\Delta\omega$>0 the per fire decrease in recruitment rate due to burning and ϕ the fire ignition rate in flammable cells. Note that, according to [10], the total flammable area is p_s = [S] + [G] (i.e., the area of grass and savanna saplings). The reasoning is that there are on average $\phi N p_s$ ignitions, each causing a fire that on average affects a proportion $\langle Q_{p_b}(p_s)\rangle$ of flammable cells, thereby lowering the recruitment rate by an amount $\Delta\omega$. If [S] and [T] cells are well-mixed (uniformly randomly distributed) in the area affected by fire, then it follows that the recruitment rate is $\omega(p_b, p_s)$[S].

For the approximate effect on forest trees [as included in 9], one needs to take into account that forest trees are assumed [in 9] to block fires perfectly. Therefore, they are not in the flammable part of the landscape, but instead share an interface with it. The mean-field rate of forest loss due to fire during a small time interval is then $\zeta(p_b, p_s)$[F],

where ζ is

$$\zeta(p_b, p_s) := 4\phi N p_s^2 p_{\mathrm{f}} \langle Q_{p_{\mathrm{b}}}(p_s)\rangle, \tag{S26}$$

with $p_s = [\mathrm{S}] + [\mathrm{G}]$ also. The reasoning here is as follows. There are on average $\phi N p_s$ ignitions, each causing a fire that affects a proportion $\langle Q_{p_{\mathrm{b}}}(p_s)\rangle$ of the landscape. Assuming burnt cells and forest cells are well-mixed, such that there is no correlation between them, one can write the interface between them as the number of forest-burnt pairs in a lattice: $4(\langle Q_{p_{\mathrm{b}}}(p_s)\rangle p_s)[\mathrm{F}]$. For each such pair, there is a probability p_{f} of spreading into forest, such that (when using the approximation of small p_{f} as in the main text), the resulting forest loss is $4\phi N p_s^2 p_{\mathrm{f}} \langle Q_{p_{\mathrm{b}}}(p_s)\rangle[\mathrm{F}]$.

For large domains, one may replace $\langle Q_{p_{\mathrm{b}}}(p_s)\rangle$ by the percolation probability $P_\infty(p_b, p_s)$ (shown in Fig. S12a), which is the probability that a flammable cell is part of the giant connected component.

S7. ADDITIONAL FIGURES

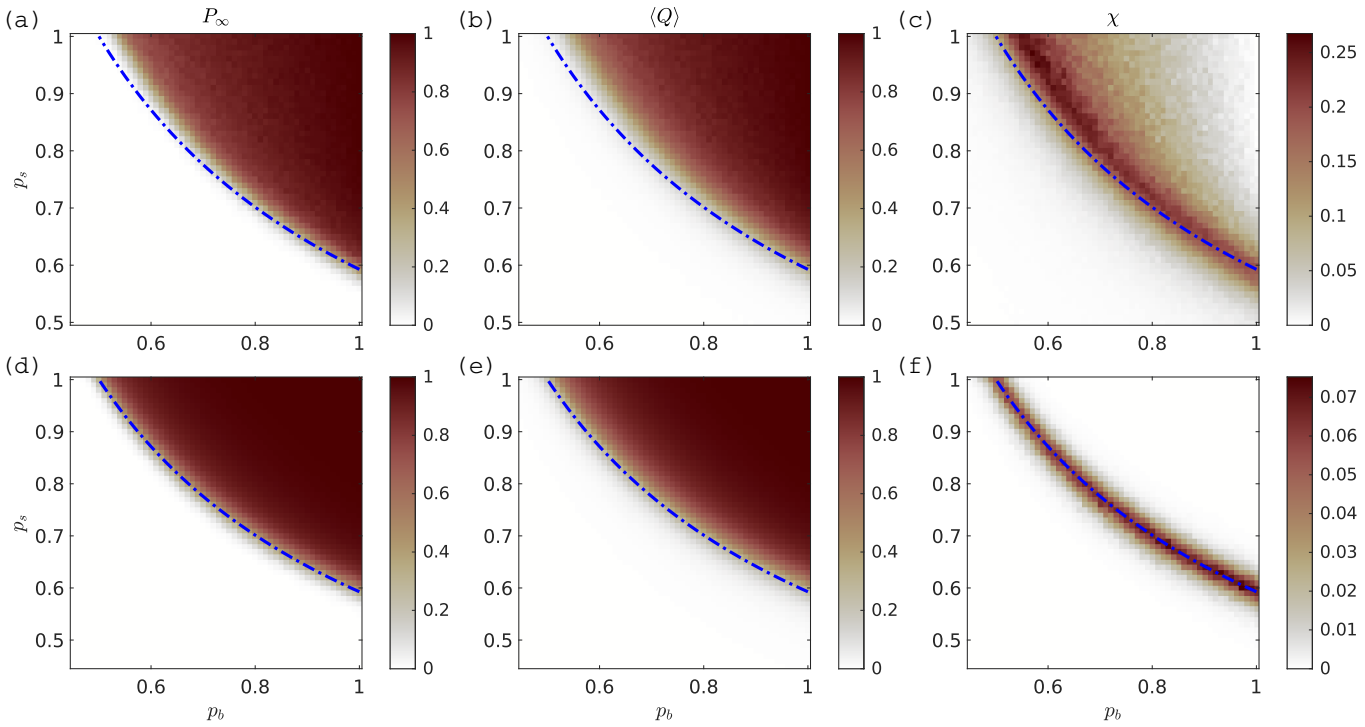

FIG. S12. GBA process with ϕ=λ=0 (equivalent to SIR spreading on the square lattice) in terms of bond occupation probability $p_b := p_g$ (Eq. 3) and site occupation probability $p_s := [G]_0$ (a-c) and compared to standard mixed site-bond percolation (d-f). Shown quantities as a function of bond and site occupation probability (based on 1024 realisations for (a-c) and on 512 realisations for (d-f)): (a,d) percolation probability P_∞, (b,e) mean proportion of burnt grass cells $\langle Q \rangle$ (see Eq. S4), and, (c,f) susceptibility χ=$\langle Q^2 \rangle / \langle Q \rangle$. Percolation probability is defined as the probability that any grass cell belongs to the giant component [18]. Susceptibility is defined here as in [58], using Q as order parameter. The dash-dotted blue line indicates the location of the infinite-size percolation threshold for uncorrelated mixed site-bond percolation (taken from [53]). For a domain size of 100x100 cells and at the shown resolution, the percolation threshold of mixed site-bond percolation matches that of the infinite size system (f). The GBA process' percolation threshold lies at higher values (c) due to spatial correlation of p_g as explained in the text. The top row is more noisy than the bottom row because for standard mixed percolation, we were able to obtain the whole distribution of cluster sizes for a each realisation and computed their statistics using percolation theory [18], whereas for the GBA process, each simulation only resulted in one sample. The colour scale was taken from [57].

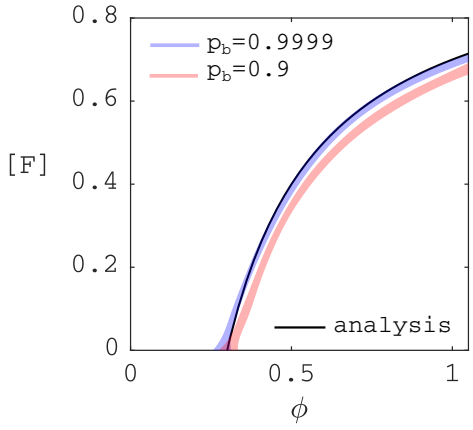

FIG. S13. Saddle of Eq. M7 via Eq. S24 (single cluster – solid black) compared to controlled simulations (shaded red: $p_g = \rho_g/(\rho_g + \mu) = 0.9$, shaded blue: $p_g = 0.9999$) in case of heterogeneous initial conditions and without spontaneous interactions (β=γ=0). Other parameters: α=0.03, ρ_f=$1.11 \cdot 10^5$, μ=10^6, λ=5.